



## **Memòria justificativa de recerca de les beques predoctorals per a la formació de personal investigador (FI)**

La memòria justificativa consta de les dues parts que venen a continuació:

- 1.- Dades bàsiques i resums
- 2.- Memòria del treball (informe científic)

Tots els camps són obligatoris

### **1.- Dades bàsiques i resums**

**Títol del projecte** ha de sintetitzar la temàtica científica del vostre document.

Implementation of zonal control algorithms in adaptive optical systems with sparse control matrices

#### **Dades de l'investigador (beneficiari de l'ajut)**

Nom: Irina  
Cognoms: Sergievskaya

Correu electrònic:  
irina.sergievskaya@cd6.upc.edu

#### **Dades del director del projecte**

Nom: Santiago  
Cognoms: Royo

Correu electrònic:  
santiago.royo@upc.edu

#### **Dades de la universitat / centre al que s'està vinculat**

Universitat Politècnica de Catalunya

#### **Número d'expedient**

**Paraules clau:** cal que esmenteu cinc conceptes que defineixin el contingut de la vostra memòria.

Enginyeria òptica, òptica adaptativa, control zonal, mirall deformable, control per blocs

#### **Data de presentació de la justificació**

27.11.2012

Nom i cognoms, i signatura del beneficiari/ària

Vist i plau del/de la director/a del projecte





---

### Resum en la llengua del projecte (màxim 300 paraules)

Miralls deformables més i més grans, amb cada cop més actuadors estan sent utilitzats actualment en aplicacions d'òptica adaptativa. El control dels miralls amb centenars d'actuadors és un tema de gran interès, ja que les tècniques de control clàssiques basades en la pseudo-inversa de la matriu de control del sistema es tornen massa lentes quan es tracta de matrius de dimensions tan grans. En aquesta tesi doctoral es proposa un mètode per l'acceleració i la paral·lelització dels algorismes de control d'aquests miralls, a través de l'aplicació d'una tècnica de control basada en la reducció a zero dels components més petits de la matriu de control (sparsification), seguida de l'optimització de l'ordenació dels accionadors de comandament atenent d'acord a la forma de la matriu, i finalment de la seva posterior divisió en petits blocs tridiagonals. Aquests blocs són molt més petits i més fàcils de fer servir en els càlculs, el que permet velocitats de càlcul molt superiors per l'eliminació dels components nuls en la matriu de control. A més, aquest enfocament permet la paral·lelització del càlcul, donant una component de velocitat addicional al sistema. Fins i tot sense paral·lelització, s'ha obtingut un augment de gairebé un 40% de la velocitat de convergència dels miralls amb només 37 actuadors, mitjançant la tècnica proposada. Per validar això, s'ha implementat un muntatge experimental nou complet, que inclou un modulador de fase programable per a la generació de turbulència mitjançant pantalles de fase, i s'ha desenvolupat un model complet del bucle de control per investigar el rendiment de l'algorisme proposat. Els resultats, tant en la simulació com experimentalment, mostren l'equivalència total en els valors de desviació després de la compensació dels diferents tipus d'aberracions per als diferents algorismes utilitzats, encara que el mètode proposat aquí permet una càrrega computacional molt menor. El procediment s'espera que sigui molt exitós quan s'aplica a miralls molt grans.





---

**Resum en anglès**(màxim 300 paraules)

Larger and larger deformable mirrors, with larger number of actuators are currently being used in adaptive optics applications. The control of mirrors with hundredths of actuators is a topic of high interest, as far as the classical control techniques based on the pseudoinverse of the control matrix of the system become too slow when so large matrices are involved. In this PhD Thesis a method has been proposed for speeding up and parallelizing the control of such mirrors, through the implementation of a control technique based on the sparsification of the control matrix, followed by the optimization of its actuator ordering according to the matrix shape, and its subsequent division into smaller, tridiagonal blocks. These blocks are much smaller and easier to manage in calculations, enabling computational speeds by the removal of the null components in the control matrix. Furthermore, this approach enables parallelization of the calculation. Even without parallelization, an enhancement of almost a 40% of the speed for mirrors with just 37 actuators is attained using the proposed technique. To validate this, a full experimental setup has been built, including a programmable phase modulator for turbulence generation using phase screens, and a full model of the control loop has also been implemented to investigate the performance of the proposed algorithm. Results, both in simulation and in experiment, show the total equivalence in the rms values after compensation of different types of aberrations for the different algorithms used, although the method proposed here enables a much smaller computational load. The procedure is expected to be much successful when applied to very large mirrors.



---

**2.- Memòria del treball** (informe científic sense limitació de paraules). Pot incloure altres fitxers de qualsevol mena, no més grans de 10 MB cadascun d'ells.

1. Introduction
2. State of the art
  - 2.1 Adaptive Optical Imaging Systems
    - 2.1.1 Basic Structure and Operation Principles
    - 2.1.2 Modal Wavefront Reconstruction and Control
    - 2.1.3 Zonal Wavefront Reconstruction
    - 2.1.4 Hierarchic Wavefront Reconstruction
    - 2.1.5 Sparse Matrix Techniques Used for Wavefront Reconstruction
  - 2.2 Control Design and Optimization of Adaptive Optical Systems
  - 2.3 Modeling and Simulation of Adaptive Optical Systems
    - 2.3.1 Piezoelectric Deformable Mirror Modeling
    - 2.3.2 Shack-Hartmann Wavefront Sensor Modeling
    - 2.3.3 Atmospheric Turbulence Modeling
3. Experimental results
  - 3.1 Experimental Setup Design
    - 3.1.1 Optical Scheme
    - 3.1.2 Control Scheme
    - 3.1.3 Wavefront Corrector
    - 3.1.4 Wavefront Sensor
    - 3.1.5 Turbulence Generator
    - 3.1.6 Experimental Setup, Measurement and Fitting Conditions
  - 3.2 Zonal control algorithm
    - 3.2.1 Sparse MIF B-spline Representation
  - 3.3 Large-scale PDM model
    - 3.3.1 Zonal Control Algorithm
    - 3.3.2 Adaptive Optical System Numerical Model and Simulations
    - 3.3.3 Experimental Implementation of Zonal and Modal Control
  - 3.4 Active control of a liquid crystal programmable phase modulator
  - 3.5 Block control algorithms
4. Present situation
5. Publications
6. Bibliography used

## 1. Introduction;

Active and adaptive optical systems are widely used in industry, medicine and astronomy. The main purposes of introducing an active module into optical channel are 1) to obtain specified intensity distribution in image plane (for example, in industrial lasers applications, optical scanning, holography production etc.) and 2) to correct aberrations introduced by other elements of imaging system or by environment into optical path. Unpredictable dynamical or a priori unknown static aberration compensation requires a wavefront reconstruction procedure prior to corrector signal generation and, for that purpose, a measurement module is normally introduced into the system in addition to the active corrector (though its presence is not always necessary, as for instance in “sensorless” adaptive optics techniques, where controller signals are based on scientific camera image analysis).

In case of dynamical wavefront compensation, the duration of the control cycle becomes one of the most important parameters for adaptive optical system performance, alongside with sensing accuracy and correction range.

Adaptive optical systems using active elements with a large number of degrees of freedom and high resolution wavefront sensors are able to provide precise correction of dynamic aberrations within a wide range of spatial frequencies. The most popular approach, modal control, requires in that case huge computing capacity for optimal correction signal calculation: modal control implies the need of considering each actuator's influence on each sensor node signal, so the number of computing operations increases as a square of the degrees of freedom (number of corrector's actuators) in the system, or as a fourth degree to pupil diameter (considering a certain density of actuators). Real time compensation of dynamically changing aberrations, such as atmospheric turbulence, shows the relevance to reduce duration of control cycle while maintaining the residual error of an open loop correction as low as possible.

Correctors with zonal type of actuator response such as piezoelectric deformable mirrors (PDM) are able to provide partially independent responses for different mirror zones. This makes possible considering a zonal correction technique which can reduce the delay due to calculations thus speeding up the whole control cycle. Zonal approach is also an opportunity for adaptive control of multiaperture optical systems or for systems with complex shape of the entrance pupil.

In this work zonal methods of wavefront reconstruction and correction are studied, and the elaboration of an efficient block matrix-shaped zonal control algorithm is the main goal of the project. The possibility of using piezoelectric deformable mirror for zonal control is to be experimentally studied as far as actuators' response locality is believed to be a key factor for both correction accuracy and computation efficiency. In particular, the closed loop feedback control case will be considered for its advantage of having weak sensitivity to hardware non linearity aspects such as, for instance, hysteresis. Stability properties of control system should also be considered thus. The has been supported with stays at National University of Ireland at Galway, with the group of Professor Chris Dainty, where a one-month stay was performed to gain better knowledge of the state of the art of these systems, and to gain knowledge and workbench experience from this team in control system design and optimization for adaptive optical systems.

The **main result obtained** in the PhD has been the development of a zonal control approach based on the use of **block sub-matrices** for inversion of the matrix of influence functions using least squares approach instead of the classical pseudoinverse methods. The method has been numerically and experimentally tested and especially promising for large adaptive optical systems with high resolution of corrector and wavefront sensor, where a local approach for a deformable mirrors with very large number of actuators, where the inversion of the matrix of influence functions is not feasible. Please notice that experimental, off-the-shelf deformable mirrors with over 1000 actuators are already in the market, following the trend of higher accuracy compensation of wavefront modes.

Thus, a method which takes advantage of the sparsity of the matrix of influence functions, which inverts the matrix using a block strategy (the matrix is divided into independent diagonal blocks which may be processed in parallel) has been proposed, implemented and tested experimentally in the lab. Results show the experimental equivalence regarding accuracy of the block method proposed when compared with the results obtained using the classical methods of matrix inversion, like pseudoinverse or least squares, both in simulated and experimental situations. The model validity has been experimentally proved on a more modest adaptive optical system using commercial components. Different dynamic random aberration generators were implemented to simulate atmospheric turbulence, with flexible temporal and spatial statistical parameters, including a liquid crystal programmable phase modulator, and a low-speed turbulence generator enabling real time correction (for low speed aberrations).

## 2. State of the art

Three main topics are to be covered in current chapter, corresponding to the main areas covered in the proposed project: adaptive optical system principles, control design issues for adaptive optics, and numerical modeling of adaptive imaging system including piezoelectric deformable mirror, wavefront sensor and turbulence phase screen modeling and simulation.

Basic structure of adaptive optical imaging system (AOIS), principles of its operation and main functions of elements are presented in this review. Special attention is paid to the techniques of wavefront reconstruction and control, their accuracy, calculation volume scaling and on overall efficiency for adaptive systems with a large number of actuators. Modal control, the classical approach used in a vast majority of modern adaptive systems is described briefly. Zonal wavefront reconstruction techniques and its advantages for high spatial frequency representation are then portrayed. Hybrid approaches, such as hierarchic reconstructors, combining advantages of zonal and modal techniques, are also reviewed for completeness. Wavefront reconstructors exploiting the advantages of the calculation of sparse matrices (matrices with a large number of neglectable elements) are an interesting starting point for the elaboration of zonal control algorithm. The accuracy of sparse controllers and its scaling properties are illustrated in numerous reports. Both least square solutions and minimal variance reconstructors using sparse matrices are widely used in modern large adaptive optical systems. As far as sparse operations are more an issue on how they are programmed, they will be just mentioned here without a detailed description, which can be found in cited papers, which are extended works on applied mathematics.

As a second area of interest, basics of closed loop system description and optimization in control theory terms are briefly reviewed. The transfer functions of the involved individual components are presented. A method for analysis of stability is mentioned as a necessary part of the closed loop adaptive system design process. Predictive control techniques successfully used for atmospheric turbulence compensation are also mentioned as an existing technical solution permitting open loop residual error reduction. Hysteresis pre-compensation methods are also presented due to the relatively significant hysteresis of the available deformable mirror.

Finally, the third part of review covers numerical simulation of adaptive optical systems. Mathematical models of piezoelectric deformable mirror, Shack-Hartmann wavefront sensor and turbulence wavefront deformation are to be implemented into adaptive system model. Linear DM model with zero hysteresis is to be described. Thin plate mechanical model is chosen for DM response functions calculation. The problem of turbulence compensation is one of the most relevant ones in real time adaptive optics engineering. The demand of high resolution and fast random changes requires accurate reconstruction, and fast and flexible correction in such systems, optimization of the whole control cycle. An atmospheric turbulence model implemented in the experimental setup seems to be the optimal approach for estimating the efficiency of real time control algorithms. For that reason existing models with experimentally proved veracity have been studied. The implementation of a fast turbulence screen generator is one of the most important problems in adaptive optics simulations, several works on that question are mentioned here.

## 2.1 Adaptive Optical Imaging Systems

### 2.1.1 Basic Structure and Operation Principles

Adaptive optical imaging systems (AOIS) must be able to perform at least two main tasks: sense the deformations of the incoming wavefront, and compensate these deformations in a real-time operation mode, typically to deliver an aberration-free image on a science camera.

The basic structure of a typical AOIS includes a wavefront sensor (WFS), a wavefront corrector (deformable mirror for instance) and a control computer for actuator commandment (Fig 2.1).

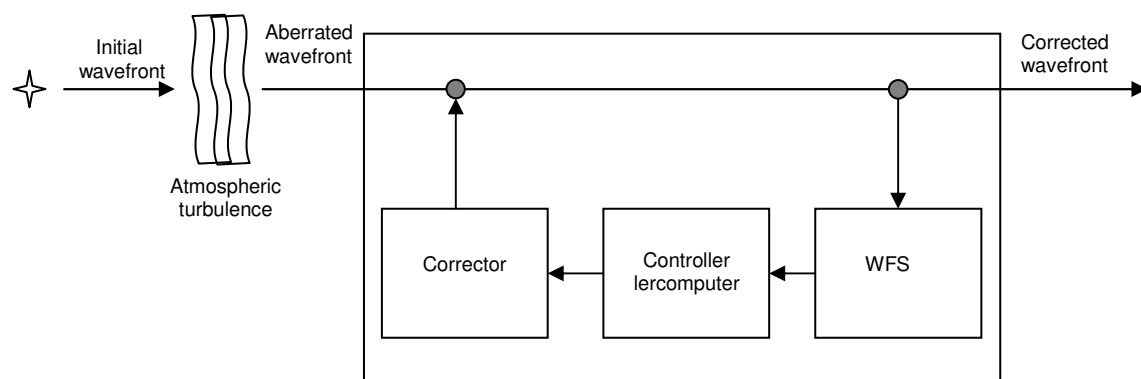


Figure 2.1: Adaptive optical imaging system.

The performance capabilities of AOIS are defined by the combination of all its components. There are several special factors that should be specially taken into account [Roggemann 1996]:

- finite light levels in the WFS
- finite spatial sampling of the WFS
- finite number of degrees of freedom available from the wavefront corrector
- finite temporal response of the AOIS

First to third factors depend on available equipment characteristics and not always can be optimized in a real system. The last factor can be divided into hardware temporal behavior and control algorithm speed and accuracy. Thus, optimization of the control algorithm is one of the most important parts of a successful AOIS design.

Wavefront reconstruction is the process of restoring the phase values within the aperture from the measured data. It is normally the first task to be performed. The tasks performed by an adaptive optics wavefront reconstruction unit are summarized as follows [Hardy 1998]:

- estimation of the overall wavefront values using zonal or modal fitting;
- removal of unnecessary components, such as piston, from the reconstructed

wavefront;

- estimation of low-order wavefront modes, such as the overall tilt and defocus components, which can be compensated separately;
- removal of cross-coupling effects caused by actuator influence functions, which would otherwise cause instability in the feedback loop;
- improvement of the noise performance by using the statistics of the wavefront being corrected in the reconstruction process;
- minimization of the error in the reconstructed wavefront by accounting for the signal-to-noise ratio of each gradient input;
- accommodation of different actuator geometries for the gradient sensor and the corrector.

Local wavefront slope measurements are distorted by random noise present in the WFS, meaning that spatial integration through different paths will never produce equal wavefront phases, so a statistical approach for the solution is required. The most usual approach for wavefront fitting is minimization of the mean-square error between the reconstructed wavefront and the measured gradients (least square solution, LSS) [Fried 1977], [Southwell 1980]. Minimum variance reconstruction is also a popular method widely used for control of multi-conjugate adaptive optical systems [Ellerbroek 1986], [Gilles, 2003].

Regarding compensation, control algorithms are normally separated into three groups, depending on the type of wavefront representation used for reconstruction:

- modal control algorithms,
- zonal control algorithms,
- hierarchic control algorithms.

In modal algorithms the aberrated wavefront measured with the wavefront sensor is represented as a weighted sum of modes, each of them defined over the whole pupil. In case of an orthogonal modal basis, optimal correction is achieved by independent correction of each mode. Modal algorithms provide smooth reconstructed wavefronts with high stability to the noise in sensor slope measurements. Reconstruction over the basis of corrector response functions provides optimal correction control signals as coefficients of the derived basis functions [Wallner 1983].

Zonal algorithms are based on independent correction of wavefront zones relying on local wavefront sensor data [Southwell 1980]. Usually, zonal algorithms are combined with modal tilt/defocusing estimation and independent compensation. Zonal algorithms are able to provide a phase map representing local features with more accurate definition but have higher error propagation coefficient, meaning that sensor noise can produce significant errors in low order aberration components [Miller 1999], [Panagopoulou]. An important advantage of zonal algorithms is the reduced number of operations required to get a reconstruction.

Fig.2.2 illustrates quite clearly the difference in modal and zonal wavefront reconstructions of the same wavefront.

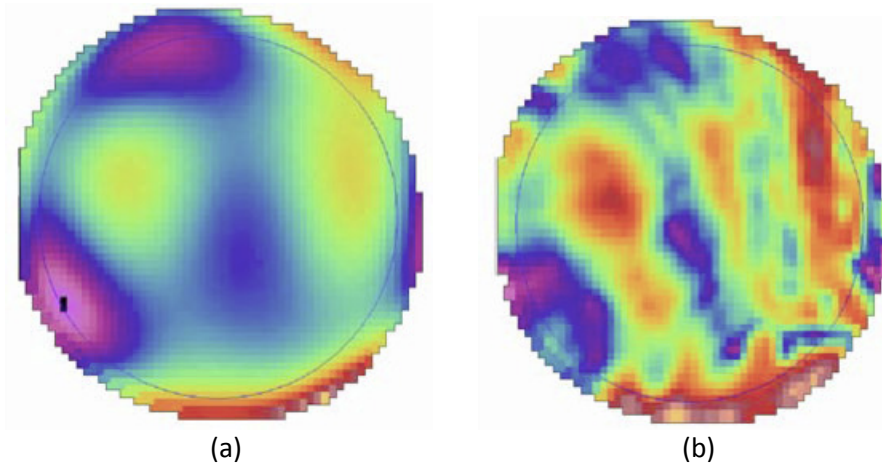


**Figure 2.2** Modal (a) and zonal (b) methods for wavefront reconstruction [Panagopoulou]

In hierarchic algorithms local approximations are used together with more extended zonal or modal components for combining fitting accuracy of low order modes and a reduced number of calculation operations [MacMartin 2003].

### 2.1.2 Modal Wavefront Reconstruction and Control

In a modal approach, a wavefront is described in the form of an expansion of orthogonal functions [Southwell 1980]:

$$\phi(x, y) = \sum_{k=0}^M a_k n_k F_k(x, y), \quad (1)$$

where  $F_k(x, y)$  are the two-dimensional functions orthogonal over aperture,  $a_k$  – weighting coefficients and  $n_k$  provide normalization. It is convenient to normalize  $F_k$  in such a way that the phase variance has a simple expression:

$$\sigma_\phi^2 = \sum_{k=1}^M a_k^2. \quad (2)$$

The wavefront slopes are then obtained by differentiation:

$$\begin{aligned} S^x &= \sum_{k=1}^M a_k n_k \frac{\partial F_k}{\partial x}, \\ S^y &= \sum_{k=1}^M a_k n_k \frac{\partial F_k}{\partial y}. \end{aligned} \quad (3)$$

or, in a matrix form,

$$S = Aa, \quad (4)$$

where  $A$  is a rectangular matrix with  $M$  columns and  $2m$  rows, being  $m$  the number of nodes (the number of sampling points) in a wavefront sensor, and  $a$  is a vector containing the weights given to each of the modes in the basis.

Using singular value decomposition (SVD) process [Chanan 2004], a least square solution can be found for coefficients  $a_i$  in the form of

$$a = (A^T A)^{-1} A^T S. \quad (5)$$

It is appropriate to mention that there is no error propagation in modal reconstruction algorithms. Noise averaging over nodes makes modal reconstruction stable with respect to measurement errors.

The main problem of the modal reconstruction approach is the large amount of data required and the heavy matrix multiplications involved. Parallel computing processors are used for real time control in high frequencies [Truong 2002].

One of the most popular bases for modal reconstruction is Zernike basis. Zernike polynomials are defined over the unit pupil in polar coordinates as:

$$W(\rho, \vartheta) = \sum_{n=0}^k \sum_{m=0}^n \sqrt{(n+1) \cdot (2 - \delta_{0l})} a_{nm} Z_n^l(\rho, \vartheta) = \sum_{i=1}^L a_i Z_i(\rho, \vartheta),$$

$$l = n - 2m$$

$$Z_n^l(\rho, \vartheta) = \begin{cases} R_n^l(\rho) \cos(l\vartheta), & l \leq 0 \\ R_n^l(\rho) \sin(l\vartheta), & l > 0 \end{cases}, \text{ where } 0 \leq \rho \leq 1 \text{ and } 0 \leq \vartheta \leq 2\pi, \quad (6)$$

$$R_n^l(\rho) = R_n^{n-2m}(\rho) = \sum_{s=0}^m (-1)^s \frac{(n-s)!}{s!(m-s)!(n-m-s)!} \rho^{n-2s}.$$

The first Zernike mode, corresponding to  $n=0$ , is referred to as the piston term. Wavefront sensors used in AOIS are not sensitive to the piston term, so it can be excluded from the basis.

The relationship between measured slope data and the optimal wavefront reconstruction using a Zernike polynomial basis becomes an overdetermined system of equations given by

$$\begin{pmatrix} \frac{\partial Z_1}{\partial x}(x_1, y_1) & \frac{\partial Z_2}{\partial x}(x_1, y_1) & \cdots & \cdots & \frac{\partial Z_L}{\partial x}(x_1, y_1) \\ \vdots & \ddots & \cdots & \cdots & \vdots \\ \frac{\partial Z_1}{\partial x}(x_N, y_N) & \frac{\partial Z_2}{\partial x}(x_N, y_N) & \ddots & \ddots & \frac{\partial Z_L}{\partial x}(x_N, y_N) \\ \frac{\partial Z_1}{\partial y}(x_1, y_1) & \frac{\partial Z_2}{\partial y}(x_1, y_1) & \ddots & \ddots & \frac{\partial Z_L}{\partial y}(x_1, y_1) \\ \vdots & \ddots & \ddots & \ddots & \vdots \\ \vdots & \cdots & \ddots & \ddots & \vdots \\ \frac{\partial Z_1}{\partial y}(x_N, y_N) & \frac{\partial Z_2}{\partial y}(x_N, y_N) & \cdots & \cdots & \frac{\partial Z_L}{\partial y}(x_N, y_N) \end{pmatrix} \cdot \begin{pmatrix} a_1 \\ \vdots \\ \vdots \\ \vdots \\ \vdots \\ \vdots \\ a_L \end{pmatrix} = \frac{1}{f'} \begin{pmatrix} TA_x(x_1, y_1) \\ \vdots \\ TA_x(x_N, y_N) \\ \vdots \\ TA_y(x_1, y_1) \\ \vdots \\ TA_y(x_N, y_N) \end{pmatrix}, \quad (7)$$

where coefficients  $a_i$  represent the measured wavefront in the Zernike basis and are normally computed as some type of least square solution.

Using control matrix (direct sensor slopes data for each actuator response function) instead of Zernike derivatives matrix will give us coefficients corresponding to actuators commands for best wavefront compensation [Wallner 1983].

Modal reconstruction is especially effective for wavefronts with predominant low order aberrations. In adaptive systems using compensators with global actuator responses (like, for instance, membrane mirrors), modal control is optimal for accurate correction as control matrix is fully populated.

Pupil shape should be taken into account when dealing with modal bases orthogonality. For example, Zernike basis is not orthogonal for pupils with central obscuration, rectangular shape etc.

Calibrating actuator response functions provides reconstruction taking into account spatial matching sensor and corrector and real operation conditions. Matching sensor with corrector can also improve sensitivity of system. A method of sensor matching by response functions matrix condition number minimization is proposed in [Dubra, 2007].

### 2.1.3 Zonal Wavefront Reconstruction

As in modal reconstruction the wavefront is described with a set of coefficients representing modes which extend over the whole pupil, in zonal approaches certain coefficients describe the wavefront locally, just over a limited zone [Southwell 1980].

Zonal reconstruction is effective for wavefronts with significant aberrations in spatial frequencies comparable with wavefront sensor nodes' spatial frequency, and for control in adaptive systems using deformable mirrors having local actuators' responses, such as piezoelectric mirrors, when the control matrix is sparse. In **Fig. 2.3** a control matrix having sparse structure is shown for an adaptive optical system using a DM with local actuator response [Shi 2002].

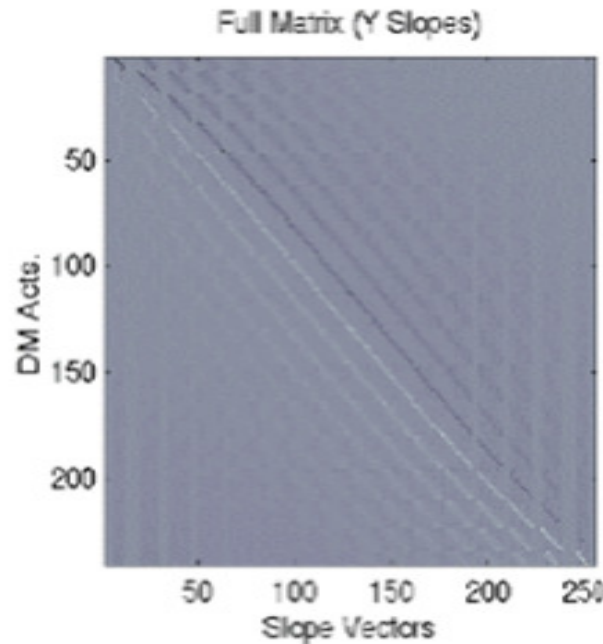


Figure 2.3 Sparse Control Matrix, [Shi 2002]

In zonal reconstruction algorithms it is usual to extract modal components such as overall tilt from wavefront before reconstruction. Tilt components can be extracted by averaging the x-tilt and y-tilt measurements from slope data. So far a matrix with removed tilt and tilt values can be calculated and applied for simultaneous correction by tip-tilt mirror and deformable mirror separately.

Simple zonal wavefront representation as a biquadratic spline can be found in [Southwell 1980]. It assumes wavefront phase in a certain zone of the wavefront sensor in x direction to be represented as:

$$\phi = c_0 + c_1 \cdot x + c_2 \cdot x^2 \quad (8)$$

Classical zonal reconstruction has high error propagation coefficient, as noise neutralization does not occur as in modal algorithms. B-spline fitting can be used for wavefront reconstruction [Ares 2006] as an alternative solution. B-spline reconstruction can not be classified as being purely modal or zonal, as basis functions have certain extension over pupil area, which is determined by the order of the B-spline basis used. B-spline basis functions can be described as a product of one-dimensional B-splines in x and y directions:

$$W(x, y) = \sum_{i=0}^n \sum_{j=0}^m b_{ij} B_{i,k}(x) B_{j,l}(y) \quad (9)$$

B-spline basis functions are defined recursively, and its shape and extension depends on the degree of spline defined:

$$\begin{aligned}
 B_{i,k}(x) &= \frac{x-t_i}{t_{i+k-1}-t_i} B_{i,k-1}(x) + \frac{t_{i+k}-x}{t_{i+k}-t_{i+1}} B_{i+1,k-1}(x) \\
 B_{i,1}(x) &= \begin{cases} 1, & t_i \leq x \leq t_{i+1} \\ 0, & \text{otherwise} \end{cases}
 \end{aligned} \tag{10}$$

One dimensional B-spline basis functions of degrees from 1 to 4 are shown in **Fig. 2.4**. Each basis function is defined only over a subdomain, and the degree of the polynomial increasing carries on extending the basis function to a larger number of neighboring subdomains.

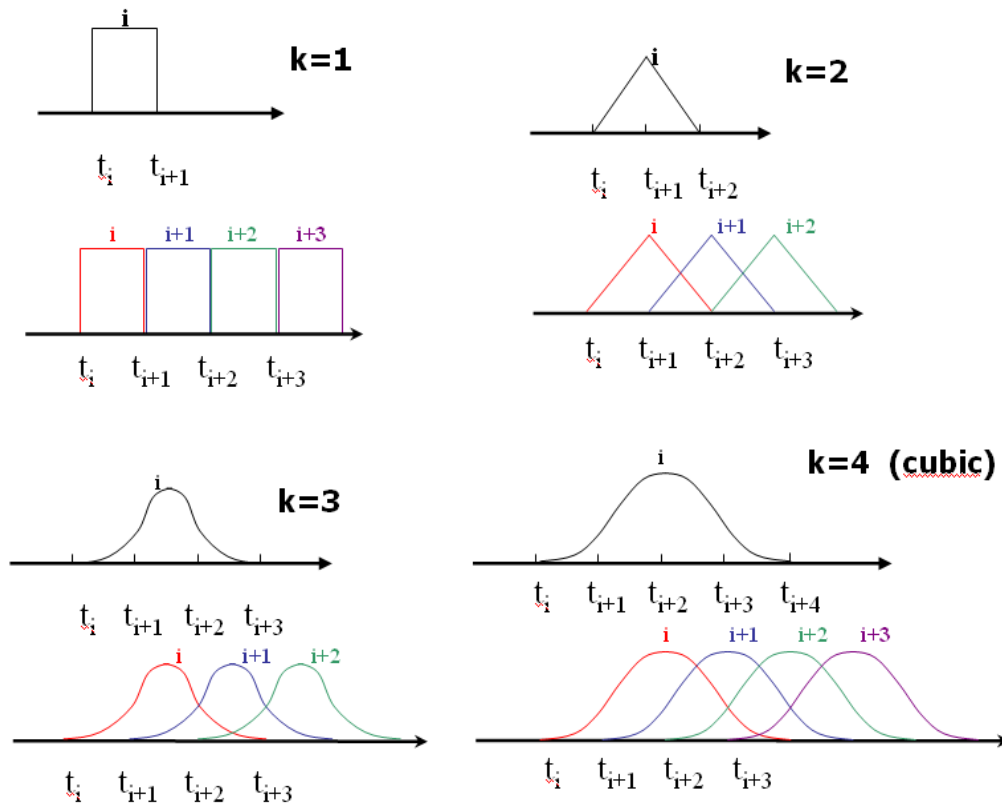


**Figure 2.4** B-spline bases of degrees 1 to 4.

It is shown in [Ares 2006] that B-spline reconstruction provides higher accuracy in terms of RMS fitting error against Zernike modal reconstruction when applied to complex wavefronts.

Error propagation in B-spline reconstruction depends on extension of basis functions. Increasing degree of B-splines leads to global behavior of basis, and subsequently to reduction of error propagation and more stable control routines.

#### 2.1.4 Hierarchic Wavefront Reconstruction

The problem with low-spatial frequencies in zonal control can be overcome by using hierarchic reconstruction algorithm [MacMartin 2003]. In two-layer hierarchy it is proposed to use one layer containing global component information from a reduced set of data, besides a second layer using zonal reconstruction and zones equal to global layer's

superelements. Using layers of similar structure allows extending algorithm for using multiple layer architecture. With  $D \times D$  Shack-Hartmann subapertures, up to  $\log_2 D$  layers of hierarchy can be included, and for a number of layers equal to  $\log_2 D$  the number of operations grows linearly to the number of nodes. **Fig. 2.5** shows simulated performance depending on number of operations for pure local, hierarchic and iterative control.

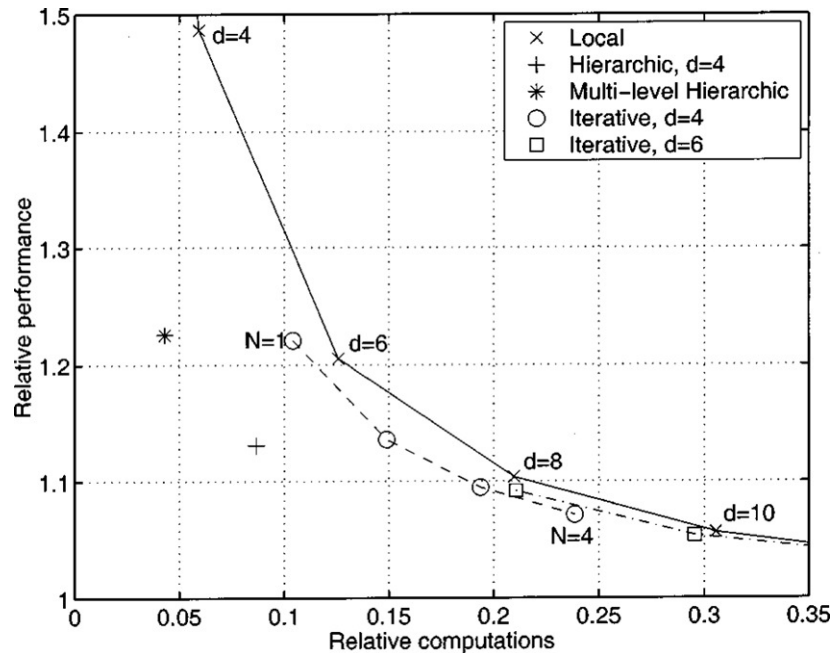


Figure 2.5 Control performance for different zonal methods [MacMartin 2003].

### 2.1.5 Sparse Matrix Techniques Used for Wavefront Reconstruction

The advantage of having sparse control matrix structure can be used for reducing computational load in reconstruction process [Wild 1995]. For instance, iterative methods are useful for solving equation reconstruction for large arrays, when matrix  $(A^T A)$  is widely sparse [Axelsson 1977]. While the number of operations of a full matrix least square solution is scaled by a square of data nodes, sparse banded calculations are scaled by the order of first degree to the number of nodes, and accepting some approximations on the structure function of the turbulence [Ellerbroek 2002], they can be also used for minimum-variance reconstructions [Gilles 2003], [Ellerbroek 2003].

According to [Murphy 2001], the sparse approach can provide an enhancement factor of 50 in the speed of reconstruction for an adaptive optical system consisting of a primary segmented mirror (7 segments) and a deformable mirror with 350 actuators with performance degradation not exceeding 10%. Sparse matrix wavefront reconstruction efficiency has been investigated in [Shi 2003] with estimations of the degradation in wavefront fitting accuracy. A review of the efficiency of sparse reconstruction techniques for open loop cycle may be found at [Vogel 2004].

Operations with sparse matrices useful for efficient wavefront reconstruction are described in [Reif 1998], [Saad 2000], [Reid 2005], [Vuik 2008]. Method of bandwidth reduction for sparse matrices described in [Cuthill 1969] can be used for actuators reordering, with further matrix transformation into tridiagonal block matrix. Parallel computation using for sparse systems solution is described in [Bücker 2002]. The efficiency of sparse matrix methods can also be compared to another fast reconstruction technique using Fourier transforms [Poyneer 2002] and having a scaling factor of  $n \cdot \log(n)$  with  $n$  – number of nodes.

## 2.2 Control Design and Optimization of an Adaptive Optical System

The most common way of control implementation in adaptive systems is setting a negative feedback loop with a wavefront corrector placed before the wavefront sensor in the control chain (Fig. 2.1). Residual error after the corrector is measured with the wavefront sensor and a proportional signal is sent to the corrector for compensation. This structure does not need as high linearity in corrector response or as wide dynamic range for sensor, as required for open loop control systems.

In system optimization, it is convenient to analyze signals and functions in frequency domain, using their Fourier or Laplace transforms. Laplace transform is usually preferred in control theory because of its advantage in initial-value problems solution [Bechhoefer 2005].

Incoming dynamic aberration function  $W(t)$  will be introduced in adaptive loop as its Laplace transform:

$$L[W(t)] \equiv W(s) = \int_0^{\infty} W(t)e^{-st} dt \quad (11)$$

The new variable  $s$  is defined over a complex plane:  $s = \sigma + j\omega$ .

The transfer function of any element in the adaptive system may be evaluated as a ratio of outgoing and incoming signals defined by their Laplace transforms. Zeroes and poles of the transfer function can be used for stability analysis of element response.

Fig 2.6 shows the representation of an adaptive optical imaging system control loop. Wavefront disturbance  $W(s)$  coming into adaptive system is reduced by corrector's shape  $B(s)$  producing error signal  $E(s)$  also called residual aberration, which is measured and processed by open loop transfer function  $G(s)$  defining corrector phase map. Closed loop output  $C(s)$  in imaging systems ideally should be zero. The performance of control system is specified by  $G(s)$ , containing transfer functions of all elements of the loop.

Relation between input and output is defined [Hardy 1998] as :

$$E(s) = W(s) \frac{1}{1 + G(s)}, \quad (12)$$

Thus maximum possible  $G(s)$  should ensure wavefront error minimization.

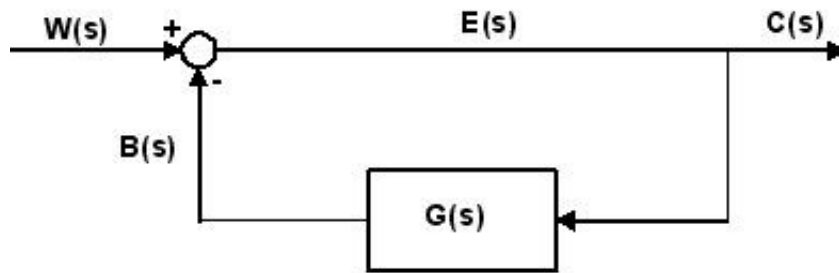


Figure 2.6 Representation of adaptive optics control system

Usually adaptive systems have more than one control feedback loops, controlling parameters such as tip and tilt, and higher-order aberrations independently. Typical transfer functions of a control loop are shown in Fig. 2.7.

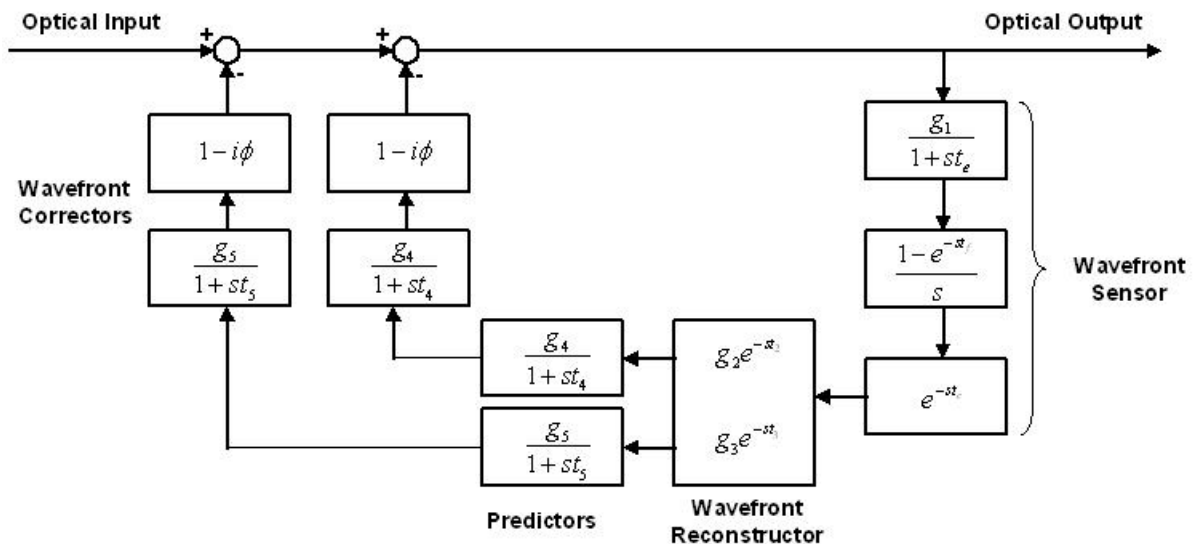


Figure 2.7 Transfer functions in a feedback control loop [Hardy 1998]

The parameters of the wavefront sensor transfer function are: transducer gain  $g_1$  (for Shack-Hartmann sensor it depends on lenslet focal length), exposure time  $t_e$  (time to collect photons, integration), readout time  $t_s$  (scanning, digitalizing and saving the whole frame), frame period  $t_f$  ( $t_f > t_s \gg t_e$ ) and wavefront processing time  $t_c$  (calculation of local wavefront tilts out of frame data). The whole wavefront sensor transfer function thus becomes:

$$G_1(s) = \frac{g_1}{1+st_e} \frac{1-e^{-st_f}}{s} e^{-st_c}. \quad (13)$$

Using “smart” wavefront sensors, having on-board processor for local wavefront tilt calculation in parallel is one of the ways to provide essential acceleration of the wavefront recognition process. [Raymond 2008].

The reconstructor can be described as the transfer functions of the two tilt calculations and multiple high-order aberrations calculations in parallel, with gain for each wavefront correction channel  $g_2$  and gain for each tilt correction channel  $g_3$  :

$$\begin{aligned} G_2(s) &= g_2 e^{-st_2}, \\ G_3(s) &= g_3 e^{-st_3}. \end{aligned} \quad (14)$$

Zero-order predictor operates like integrator and transfer functions for wavefront and tilt correction with gains  $g_4$  and  $g_5$  respectively, which are:

$$\begin{aligned} G_4(s) &= \frac{g_4}{1 + st_4}, \\ G_5(s) &= \frac{g_5}{1 + st_5}. \end{aligned} \quad (15)$$

Each correction channel is described by its transducer gain, temporal bandwidth and hysteresis. Hysteresis in piezoelectric actuators can be as large as 24 percent of the displacement [Song 2009] and can significantly reduce open loop correction performance. Its transfer function is usually modeled as a phase shift. Correction transfer functions for higher order aberrations and tilt channels are:

$$\begin{aligned} G_6(s) &= \frac{g_6}{1 + st_6} (1 - \phi_h), \\ G_7(s) &= \frac{g_7}{1 + st_7} (1 - \phi_h). \end{aligned} \quad (16)$$

With  $\phi_h$  the equivalent phase change due to the effect of hysteresis. Piezoelectric hysteresis pre-compensation can reduce its effect by 80 % and improve open-loop control (Fig 2.8), can also be useful in closed-loop systems. The overall transfer function for tilt and aberrations control channels is the product of the transfer functions of all the involved components. The frequency response determined by overall transfer function makes it possible to analyze stability of the system and overall gain function.

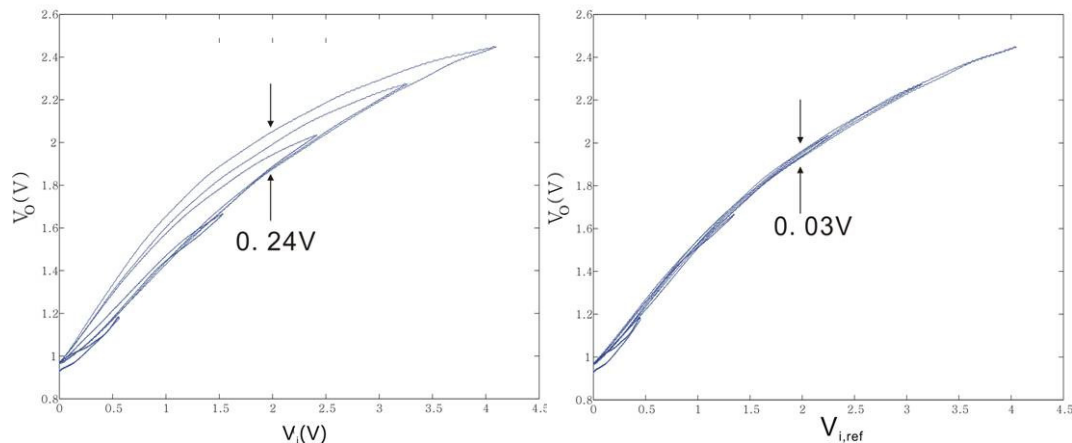


**Figure 2.8 Hysteresis in open-loop control system without and with pre-compensation [Song 2009]**

In multimodal or multizonal control systems channels work independently, so the analysis of the whole system can be reduced to the analysis of one single channel. Sensor to corrector alignment and calibration errors can introduce channel coupling effects which need be taken into account.

The open-loop transfer function of a system can be shown on a Nyquist diagram, a graph of  $G(s) = G(j\omega)$  on a complex plane for a frequency range  $0 \leq \omega \leq \infty$  [Hardy 1998]. For a closed-loop system the Nyquist diagram provides a criterion (the Nyquist criterion) which can be used for stability analysis of the system: given the open-loop transfer function of the system is stable, then the closed-loop system will be unstable for any encirclement of the critical point (-1) (Fig. 2.9).

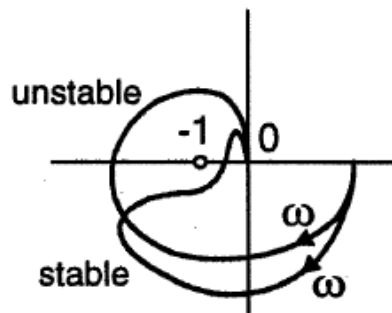


**Figure 2.9 Nyquist diagrams for unstable and stable systems [Lurie 2000]**

The Nyquist diagram does not only tell whether the system is stable or not, but also how to make the system stable by reshaping the loop response by reducing the loop gain over specific frequency range. General loop shaping methods are widely described in [Lurie 2000]. Loop shaping efficiency for adaptive optics control design has been demonstrated in [Lee 2006].

In modal control systems with separate correction for different modes it is possible to optimize each channel independently [Gendron 1994]. Control is optimized for open-loop operation of an adaptive system by using the measured aberration parameters. Independent control optimization for separate channels is also discussed in [Ellerbroek 1994].

Time delays due to image acquisition from WFS and building control command matrix through reconstruction process produce temporal errors in correction depending on wavefront dynamics. Wavefront predictions can be based on previous state of the wavefront, and on the wavefront data at near-by sub-apertures. Zero-order predictions are based on current state of atmosphere as optimal prediction for next moment. Linear predictions take into account wavefront shape in recent time. Non-linear prediction is implemented in neural network algorithms. Kolmogorov turbulence in general can be predicted with linear methods, although in some conditions the atmosphere behaves as a chaotic process, where non linear predictions can provide better performance. Under low turbulence conditions all types of predictions give comparable results.

A linear prediction method called «traveling wave predictor» is described in [Hardy 1998]. It assumes frozen turbulence structure and uses pre-calculated wind direction and velocity and previously measured wavefront for predicting new wavefront pattern correspondingly shifted to a measured one. The simulated behavior of AOIS linear predictor is presented in [Dessenne 1998]. Fig. 2.10 shows Strehl ratio vs. signal to noise ration for linear predictor and integral controller (zero-order predictor).

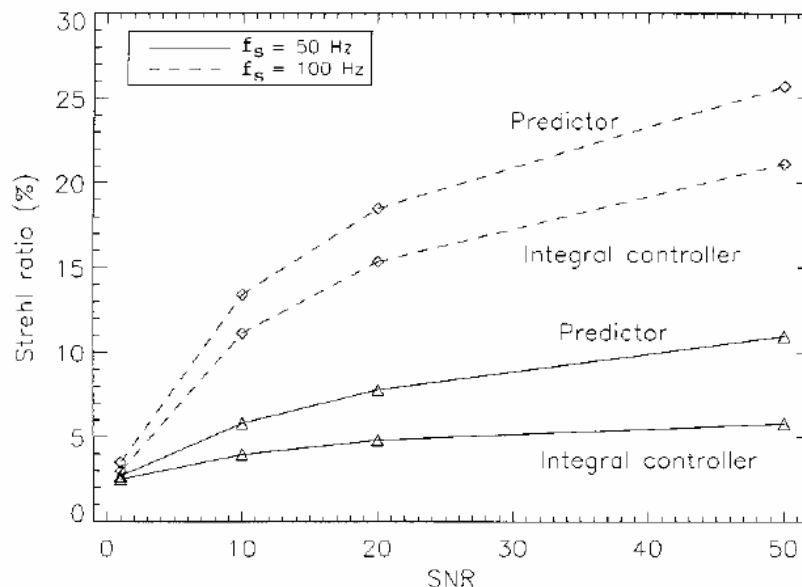


Figure 2.10: Strehl ratio vs. SNR

### 2.3 Modeling and Simulation of Adaptive Optical System

A model of an adaptive optical system should include corrector and sensor models, together with a controller model, defined by the control algorithm implemented. Random phase aberration generators with adjustable spatial and temporal statistics, and a point spread function simulator are necessary for performance evaluation. An operation counter will be introduced into the controller model for computational efficiency estimations.

#### 2.3.1 Piezoelectric Deformable Mirror Modeling

For simplicity, we will assume the wavefront corrector is supposed to have a linear response, meaning that the surface of the deformable mirror can be calculated as:

$$\hat{\phi}(\vec{x}, t) = \sum_i c_i(t) r_i(\vec{x}) \quad (17)$$

where  $c_i(t)$  is the control signal applied to  $i$ -th actuator and  $r_i(\vec{x})$  is the response function of  $i$ -th actuator.

Response functions can be measured, or calculated using a mechanical model of a mirror. For numerical simulation of the PDM behavior a thin plate bending model can be used. In this approximation, static deformation of the faceplate can be described by the biharmonic equation [Timoshenko 1959]:

$$\Delta^2 \phi(x, y) = p(x, y) / D, \quad (18)$$

$$D = \frac{E}{12(1-\nu)} h^3, \quad (19)$$

where  $\Delta$  is Laplace operator,  $p(x, y)$  is the distributed transverse load,  $D$  is the cylindrical stiffness.  $\nu$  accounts for Poisson's ratio,  $E$  for Young modulus, and  $h$  for thickness of the plate.

For a set of  $N$  actuators:

$$p(x, y) = \sum_{i=1}^N P_i \delta(x - x_i, y - y_i) S_i, \quad (20)$$

where  $P_i$  is the force applied with  $i$ -th actuator, and  $S_i$  is its section area.

A numerical solution using a finite element approach can be used; boundary conditions should be taken into account. For the case of a round plate with free edge an analytical solution exists and can be implemented for the calculation of the response functions [Loktev 2006]. This solution is cited in Preliminary Results chapter as it is used for our model. A number of more simple approximations are widely used for reducing simulation calculations. Response functions can be modeled using Gaussian or polynomial form [Tyson 2000] without taking into account position of actuator on a mirror surface. These simplified response functions can be useful for large mirror modeling, but are too rough in case of a small mirror with response functions for edge actuators different from central due to free edge effect. For our 37 actuator PDM available for experiment nearly half of actuators are in the edge.

### 2.2.2 Shack-Hartmann Wavefront Sensor Modeling

A Shack-Hartmann wavefront sensor model should include incoming phase map gradient integration over sub apertures for subsequent derivation of slope data, and a random noise generator for noise-propagation and stability analysis of the final controller. Pixelization and centroids calculation error caused by it should also be taken into account [Neal 2002]. Difficulties with Shack-Hartmann sensor modeling appear not from its mathematical evaluation, but from extremely heavy calculations and long simulation time. Hardware acceleration [Basden 2007] is able to reduce simulation time.

### 2.3.4 Atmospheric Turbulence Modeling

Due to the size of modern telescopes, atmospheric turbulence has become the most relevant limiting factor for image resolution. The main causes of turbulence are temperature inhomogeneities produced by solar heating of Earth atmosphere causing turbulent air flow. Mixing air bulks of different temperatures results in random local fluctuations in the refractive index. As a result, perfect plane wavefront from a distant star is distorted. The goal of adaptive optical systems was initially to measure and compensate wavefront aberrations caused by atmospheric turbulence.

For successful design of such a system it is important to be able to predict the effect of turbulence on the image and the corrected wavefront quality. A random aberration generator is necessary in atmospheric adaptive system design test. For correct estimations it should be based on a physical model of turbulence, having proper spatial statistics and temporal behavior.

The spatial structure of atmospheric turbulence within some range is usually described using Kolmogorov's theory [**Roggemann 1997**]:

$$\begin{aligned} \Phi_n^K &= 0.033C_n^2 k^{-11/3} \\ 2\pi / L_0 &\leq k \leq 2\pi / l_0 \end{aligned} \quad (21)$$

where  $C_n^2$  is the structure constant of index of refraction fluctuations, [ $\text{m}^{-2/3}$ ], and  $k$  is the spatial frequency [ $\text{m}^{-1}$ ]. Outer scale value  $L_0$  is of the order of tens of meters, and inner scale value  $l_0$  is of the order of a few millimeters.  $C_n^2$  is a parameter characterizing the strength of refractive index fluctuations, which depend on the turbulence layer height and on the strength of turbulence.

A proposed simple model for  $C_n^2$  is [**Ishimaru 1978**]:

$$C_n^2(z) = K_0 z^{-1/3} \exp\left(\frac{-z}{z_0}\right) \quad (22)$$

where  $K_0$  is a parameter describing the strength of turbulence and  $z_0$  is effective height of turbulent atmosphere. For atmospheric channels near ground  $C_n^2$  value can vary from  $10^{-13} \text{ m}^{-2/3}$ , for strong turbulence to  $10^{-17} \text{ m}^{-2/3}$  for weak turbulence, with  $10^{-15} \text{ m}^{-2/3}$  as a typical value [**Goodman 1985**].

To overcome problems of limited range in Kolmogorov model, can be used an alternate von Karman spectrum [**Roggemann 1997**]:

$$\Phi_n^V = \frac{0.033C_n^2}{(k^2 + k_0^2)^{11/6}} \exp\left(-\frac{k^2}{k_m^2}\right), \quad (23)$$

where  $k_0 = 2\pi / L_0$ ,  $k_m = 5.92 / l_0$ .

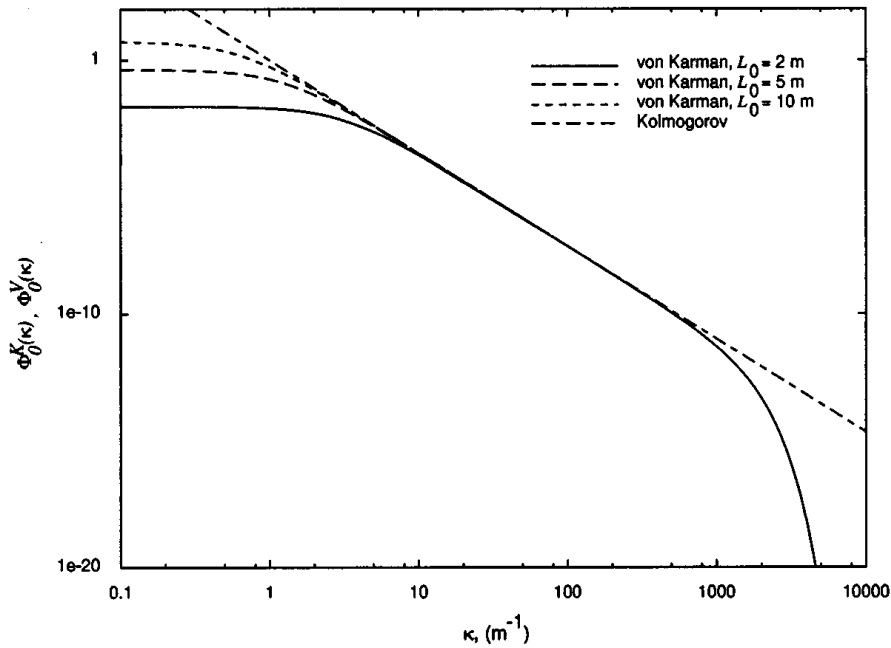


Figure 2.11 Kolmogorov and von Karman turbulence spectra [Roggemann 1997]

The Kolmogorov spectra assumption does not cover all possible turbulence statistical conditions. Representation of turbulent layers as fractal surfaces having fractional Brownian motion provides a more general model suitable for near-ground measurements [Perez 2004].

The modal method of random phase screen generation using Fourier series expansion can provide a single random phase screen with a proper spatial statistics [Welsh 1997]. This method has proved to be successful for real-time phase screen generation [Hu 2009]. In this method, the phase of the turbulence can be expressed by a Fourier series with finite terms. The coefficients of every term can be generated as independent random variables with mean square value determined by turbulence power spectrum density (PSD). Von Karman spectrum can be used as PSD model. Sparse approximation of power spectral density, with  $C_n^2 k^{-4}$  replacing  $C_n^2 k^{-11/3}$  in (21) was proposed in [Ellerbroek 2002] and clearly described in [Bardsley 2008], it may be useful for computations acceleration.

The random wavefront phase described as a Fourier series (FS) [Hu 2009]:

$$\phi_k(\vec{r}) = 2 \cdot \text{Re} \left[ \sum_{n=0}^{N-1} \sum_{n'=0}^{N-1} c_{n,n'} \cdot \exp \left\{ j2\pi \left( \frac{n\hat{x}}{D_p} + \frac{n'\hat{y}}{D_p} \right) \right\} + \sum_{n=1}^{N-1} \sum_{n'=-N+1}^{-1} c_{n,n'} \cdot \exp \left\{ j2\pi \left( \frac{n\hat{x}}{D_p} + \frac{n'\hat{y}}{D_p} \right) \right\} \right] \quad , \quad (24)$$

where  $(2N-1)^2$  is the number of terms included in the FS representation of  $\phi_k(\vec{r})$ , and  $c_{n,n'}$  is the FS coefficient, and  $\hat{x}$  and  $\hat{y}$  are unit vectors along the x and y directions, respectively.  $\vec{r} = \hat{x} \cdot m \cdot \frac{D_p}{N} + \hat{y} \cdot m' \cdot \frac{D_p}{N}$ , where  $m$  and  $m'$  are integers from 0 to N.

Uniformly spaced frequency grid results in under-representation of low spatial frequency fluctuations [Welsh 1997].

In matrix form:

$$\phi_k(\vec{r}) = 2 \cdot \text{Re} \left\{ \left( \exp(j2\pi f_x) \right)^T \cdot \left[ C_L \cdot \exp(j2\pi f_x) + C_R \cdot \exp(-j2\pi f_y) \right] \right\}, \quad (25)$$

where  $C_L$  and  $C_R$  are the matrices of dimension  $N \times N$  containing the complex random variables  $c_{n,n}$ ,  $f_x$  and  $f_y$  are spatial frequency matrices.

There are several ways to model temporal turbulence behavior. Taylor's frozen field hypothesis assumes that the whole layer moves as a monolithic block in one direction with certain velocity. Combination of shift and evolution of a phase screen gives better agreement with experimental results [**Glindmann 1993**]. Another way simulating temporal fluctuations is to use a linear combination of several screens at a moment with variable weights. The proposed option is to make a real time combination, generating a new screen for every several frames and removing the eldest screen from combination, reducing its weight smoothly. An efficient and flexible method for this is to use one dimensional B-spline basis functions for calculating the weight to be applied to a given fixed screen in a certain moment. Obviously, the sum of all weights should be equal to 1, otherwise the statistic properties of the sum will differ from the statistics of the summands.

The advantage of the proposed method is that it is not necessary to generate a random phase screen for every frame to get a continuously changing random result, so real time generation becomes possible. Proper temporal statistics can be provided by b-spline parameters such as order and control points' frequency.

Phase map as a combination of temporally weighted random screens with 1-D B-splines of order  $k$  used for weighting.

As far as phase screen generation is a quite operation consuming procedure, calculation time is usually saved using sparse random phase generation with following interpolation between generated points [**Sriram 2007**].

### 3. Results

#### 3.1 *Experimental Setup Design*

Aim of experimental setup is to provide a method of real time observation, measurement and feedback compensation of dynamically changing wavefront aberrations. This specifies presence in setup and optical conjugation of following elements: aberration simulator, wavefront sensor and wavefront compensator. Imaging camera is also useful for direct estimation of correction quality.

Preliminary design of optical scheme and control block diagram are described in this section alongside with main optical elements available for setup with their principle parameters.

##### 5.1.1 Optical Scheme

Optical scheme of proposed experimental setup is shown in **Fig. 3.1**. Collimated beam 1 is directed by beam splitter 2 to the wavefront modulator 3; after conjugating lens 4 and beam splitter 5 light is shaped by wavefront corrector 6 optically conjugated by lens 7 with separated by beam splitter 8 pupils of wavefront sensor 9 and imaging camera 10.

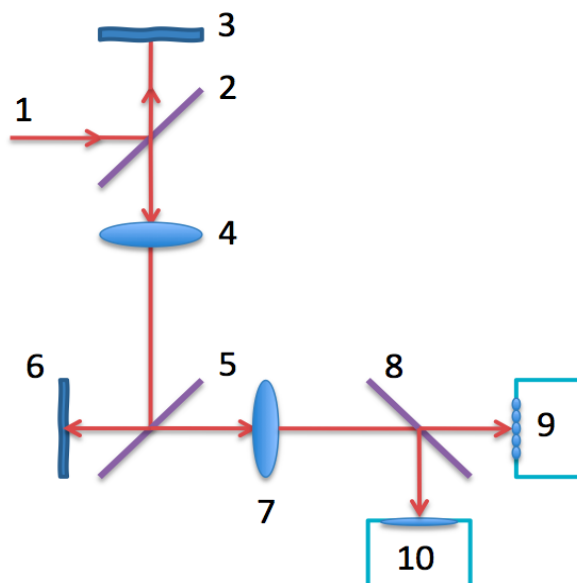


**Figure 3.1** Experimental setup: optical scheme

Parameters of elements should be chosen to meet following requirements:

- optical systems 4 and 7 magnification provide pupils conjugation with certain scale;
- focal length of imaging camera objective gives angular resolution sufficient for image quality estimation within range of aberrations generated by 3;

- dynamic range of wavefront sensor 9 and of active elements 3 and 6 ensure sensitivity of sensor to active elements response
- dynamic range of corrector 6 ensure correction of aberration introduced by correction by wavefront modulator 3.

### 3.1.2 Control Scheme

Principle scheme of setup is shown in **Fig. 3.2**. Turbulence screen is generated within needed statistical properties and collimated laser beam is shaped using modulator. Focused aberrated wavefront can be useful for turbulence generator accuracy rating and for advanced estimation of correction algorithm efficiency.

Negative feedback loop controlled independently from turbulence generator is used for correction modeling. Zonal and modal decomposition algorithms can be realized and compared in equal conditions.

Comparing corrected and aberrated image can be used as a measure of algorithm efficiency.

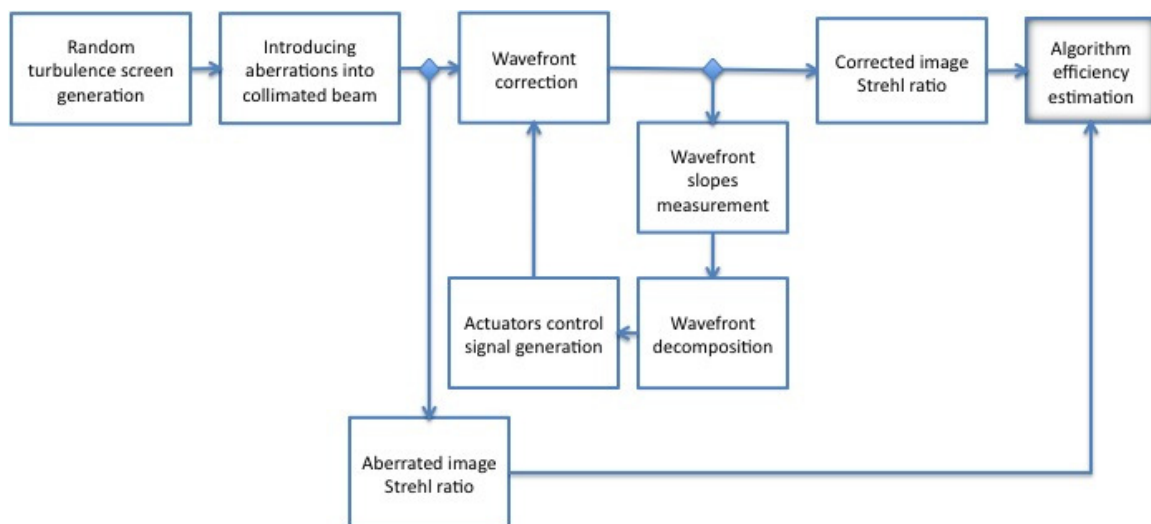


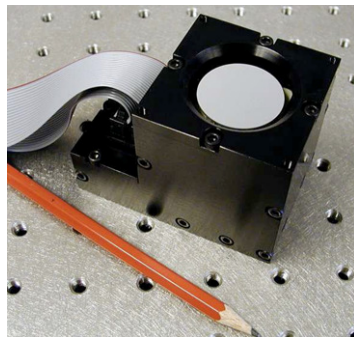
**Figure 3.2**  
**Experimental setup: control scheme**

It is supposed to use MatLab software for both hardware interfacing and decomposition calculating.

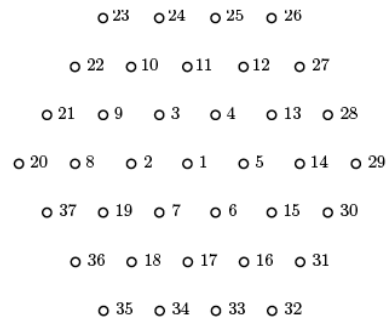
### 3.1.3 Wavefront Corrector

As a wavefront corrector, piezoelectric deformable mirror (PDM) having 37 actuators can be used. PDM 37 by OKOTech has optical diameter of 30 mm, actuators are in hexagonal pattern with pitch of 4.3 mm. Maximum actuator stroke is 8  $\mu\text{m}$ .

Appearance of PDM and it's actuators pattern are presented in **Fig. 3.3**



a



b

**Figure 3.3 PDM 37 (a) and positioning of its actuators (b)**

Due to production process initial shape of PDM has significant defocus. Measured surface shape is presented in **Fig. 3.4**. Peak to valley is 0.83  $\mu\text{m}$ , initial defocus 0.62, some spherical aberration and coma also present.

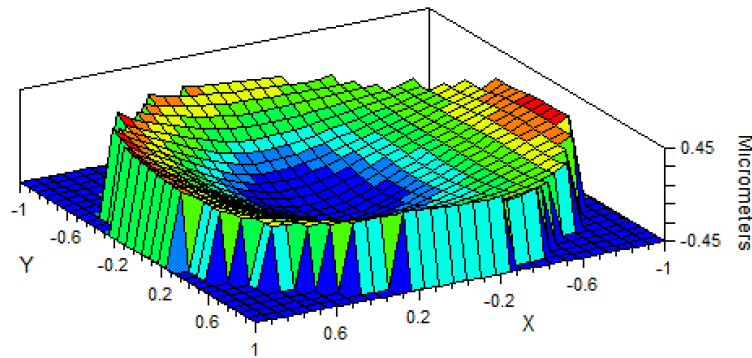


**Figure 3.4 PDM 37 initial shape**

Defocus and spherical aberration can be compensated in design of conjugation lens thus full actuator stroke can be used for symmetrical wavefront aberration compensation. Otherwise effective dynamic range of some actuators (mainly the central one) would be reduced almost twice.

### 3.1.4 Wavefront Sensor

Shack-Hartmann wave front sensor is usually used for wavefront recognition in adaptive optical systems. Principle of its operation is beam sampling by an array of microlenses, each one of them imaging focused subaperture in a position depending on local wavefront tilt (**Fig.3.5**). Light spots' coordinates deviation from ideal plane wavefront data can be used for wavefront approximation in terms of polynomials.

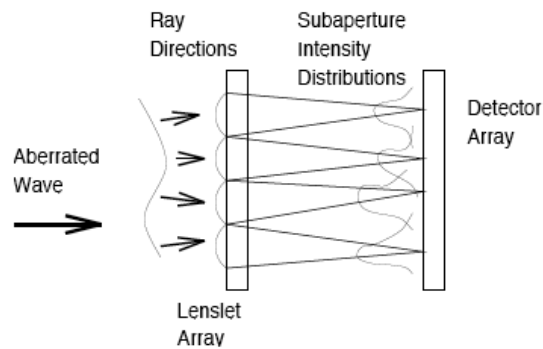


**Figure 3.5**  
**Shack-Hartmann WFS working principle**

C-Mount 1/2" CCD camera with resolution 640:480 pixels and an array of 127 microlenses with focal length of 17 mm in a hexagonal package form WFS. Working pupil diameter of microlens array is 3.8 mm. (**Fig. 3.6**). Data is transferred using USB interface.

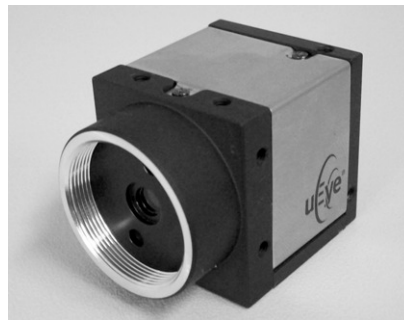


**Figure 3.6**  
**Shack-Hartmann WFS**

### 3.1.5 Turbulence Generator

Programmable Phase Modulator (PPM) is planned to be used in experimental setup as an active element introducing random dynamic aberration into the optical path. Structure of PPM is illustrated in **Fig. 3.7**.

Incoming wavefront phase is shaped by Parallel Aligned Nematic Liquid Crystal Spatial Light Modulator (PAL SLM) that is optically coupled with intensity modulator controlled from PC. PPM X8267 by Hamamatsu (**Fig. 3.8**) that is available for experiment uses monochrome liquid crystal matrix (LC) with resolution of 768 x 768 pixels controlled through VGA port and optical system for addressing PAL SLM. Optical system is used for transferring intensity pattern generated by LC onto PAL SLM. Light intensity determines produced voltage and index of refraction on SLM. Thus intensity pattern on LC is converted into index of refraction pattern in SLM. Light beam entering the PPM reflects from dielectric mirror behind liquid crystal, having a double pass through index of refraction pattern. Slight defocusing in optical conjugation smoothes initially discrete digital image to achieve an even addressing distribution on SLM avoiding diffraction and preventing efficiency losses for readout light.

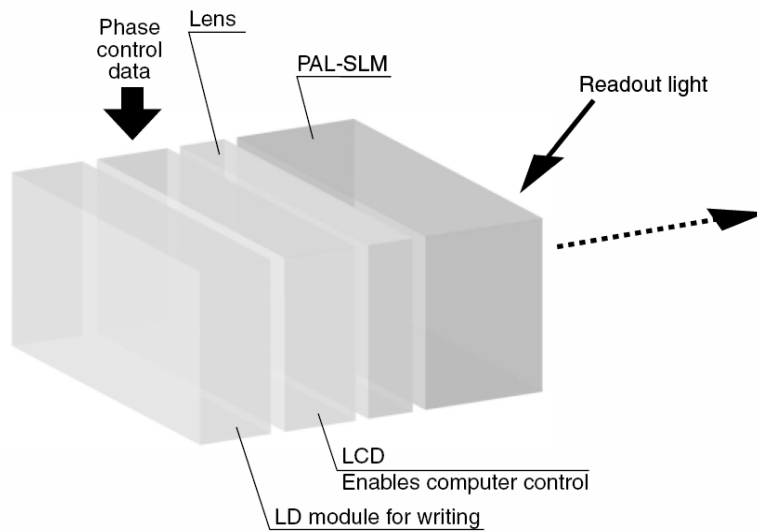


Figure 3.7 PPM Structure

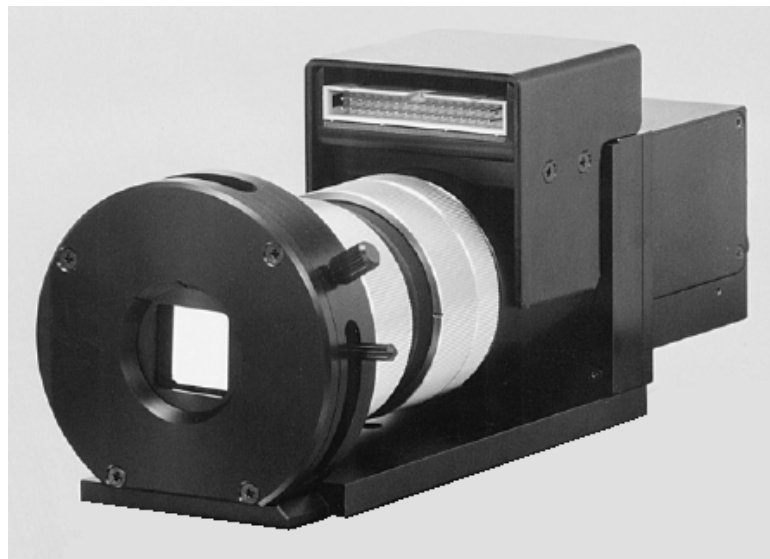


Figure 3.8 PPM X8267

Although PAL SLM transfer function is not linear, PPM precalibration allows assuming it so. Given PPM is designed for using with readout light wavelength of a visible range (400-700 nm), for 633nm readout light phase modulation level is around  $2.3\pi$  radians (Fig. 3.9).

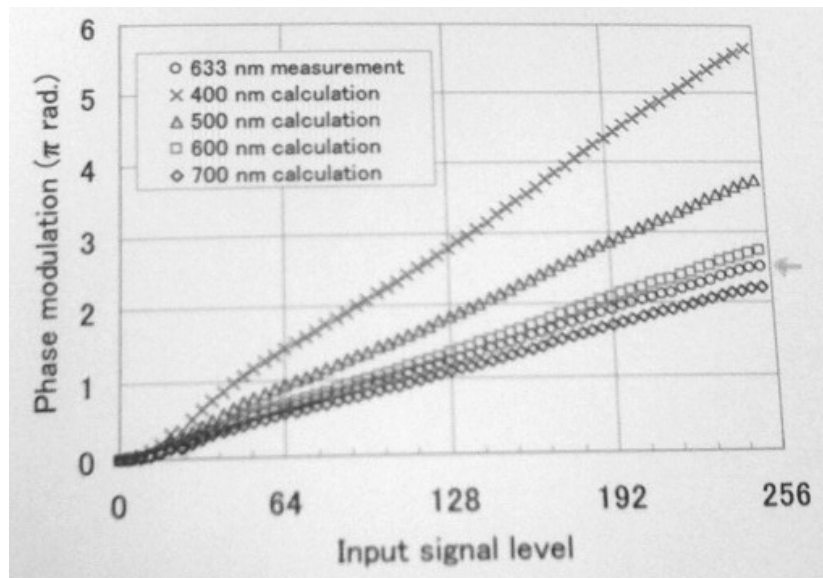


Figure 3.9 X8267 transfer function

Relatively slow response of SLM (Fig. 3.10) limits its use as an active element in real time adaptive optical systems, but 256-grey-level linear transfer characteristic with high spatial resolution allows its application in laboratory experimental setup as aberration generator.

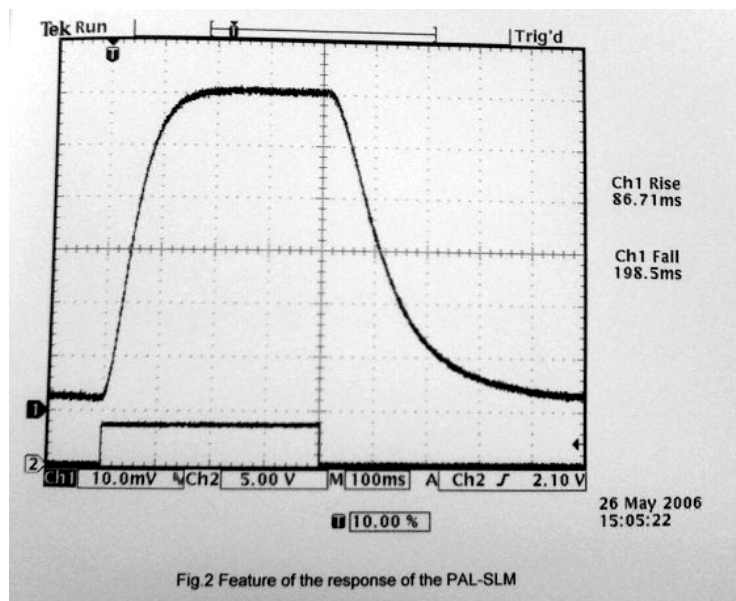


Fig.2 Feature of the response of the PAL-SLM

Figure 3.10  
PAL SLM response function

### 3.2 DM Response Measurement and B-spline Reconstruction

Zonal representation of simulated complex wavefront was studied in [Ares 2006]. It is important to examine efficiency and accuracy of zonal representation of real wavefronts

generated with PDM actuators. Mirror response functions were measured with wavefront sensor and this experimental slope data was approximated with modal and zonal polynomials. Degree of locality is estimated for actuators' response by comparing their full and sparse zonal approximation RMS. Complex wavefronts with several operating actuators were fitted with modal and zonal polynomials using comparable number of degrees of freedom. Sparse representation accuracy of PDM influence function is estimated.

### 5.2.1 Experimental Setup, Measurement and Fitting Conditions

Experimental setup consists of 37 actuators PDM mirror by OKOTech with hexagonal regular actuators pattern and 127 microlens Shack-Hartmann hexagonal sensor, conjugated with mirror using double telecentric imaging lens. Scheme of setup is presented in Fig.3.11. Optical matching of mirror and wavefront sensor is shown in Fig.3.12.

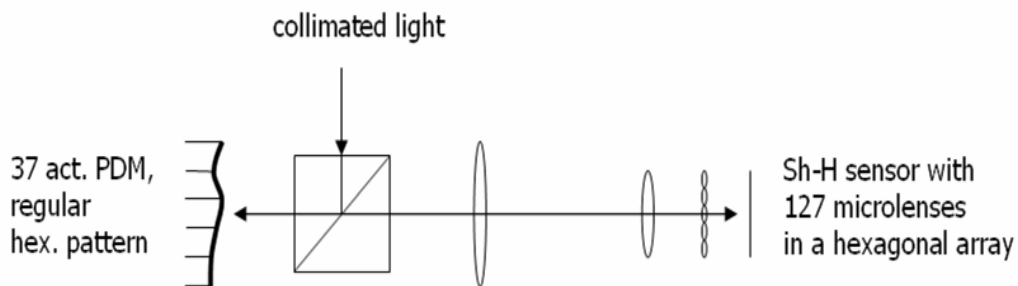


Figure 3.11 PDM response measurement: optical scheme

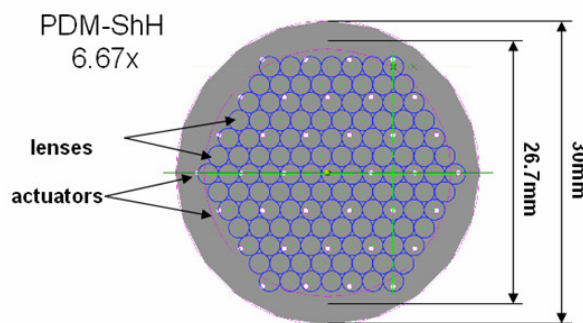
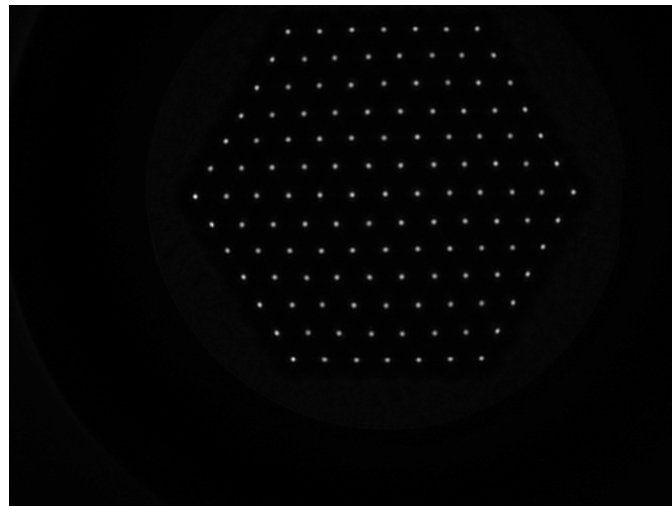


Figure 3.12 Optical conjugation between PDM and Sh-H sensor



**Figure 3.13 PDM influence functions measurement: experimental setup.**

Collimated light is shaped with PDM, local wavefront slopes are available from image (**Fig.3.14**) taken with Sh-H sensor camera.



**Figure 3.14  
Sh-H sensor image.**

Wavefront local slopes for a PDM response function are calculated as a difference between light spots centroids of patterns after and before applying control voltage. This helps to reduce hysteresis effect on PMD response and exclude optical aberrations of collimator and imaging lens from measurement.

For a single response function measurement two patterns are saved thus. An algorithm for pattern analysis and polynomial fitting is realized in MatLab computing environment, which gives high flexibility in calculations and data visualization.

For fast conversion image received from sensor camera into slopes data array initial nodes' coordinates should be known for further fast search of each node in the neighborhood of its initial position. Coordinates can be generated mathematically with known lenslet array orientation, center position and pitch. But as initial position and orientation are not known and pitch depends a lot on optical system aberrations and defocusing, it is better to find nodes coordinates experimentally saving a pattern for a wavefront with zero voltages on



PDM actuators. This process can be considered as a sensor calibration for certain microlens array orientation and individual nodes positions, and optical system aberrations. Achieved

coordinates are not used for reference, just as a start point of search process in image-to-coordinates conversion.

Sensor calibration process needs initial information: sensor camera resolution, lens array order: number of nodes in a lens array hexagon side, 7 in a given Sh-H sensor, approximate orientation of hexagon with respect to camera: horizontal or vertical. During sensor calibration process such parameters as lens array tilt and position, nodes pitch are calculated and individual nodes coordinates are found.

Full image scanning is done only during calibration. Afterwards during pattern recognition nodes are assumed to be in the neighborhood of calibration coordinates and are sought by local scanning. For measuring mirror influence functions patterns before and after control voltage is applied are compared. In other words slopes are calculated as a difference between two nodes arrays. For wavefront shape measurement nodes array is compared with pre-measured plane wavefront nodes coordinates.

Matrix of influence functions of a size  $N_a \times 2N_n$ , where  $N_a$  is the number of actuators and  $N_n$  is the number of nodes is experimentally achieved for 37 actuators PDM and it is shown in **Fig. 3.13**. Due to local character of actuator response majority of MIF elements have values close to zero.



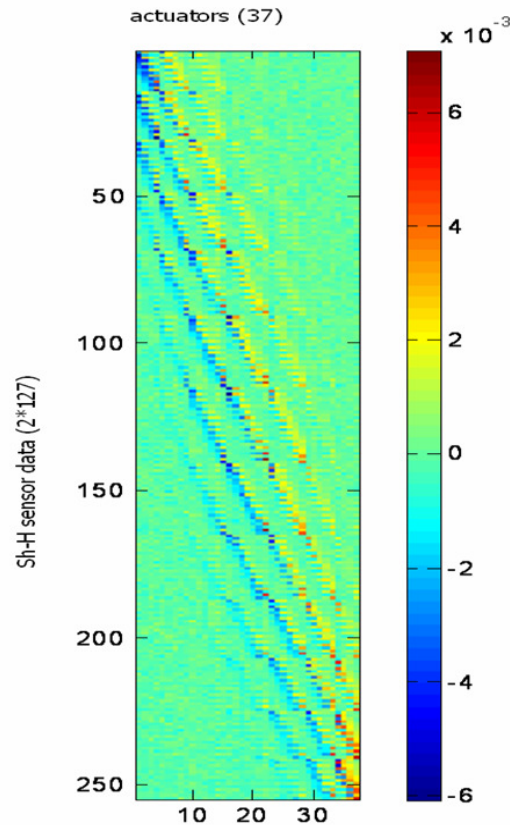
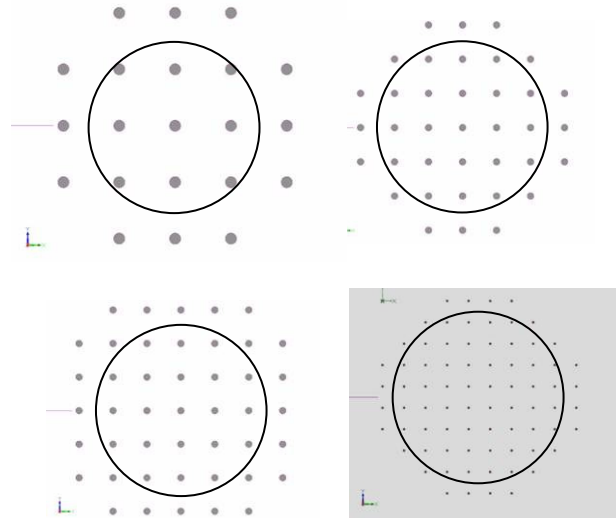


Figure 3.15 A typical sparse MIF made with mirror modes

For wavefront recognition in systems using a mirror like PDM with a local behavior of actuator response zonal decomposition can have an advantage comparing to modal one with same number of freedom degrees. Comparison between Zernike modal and B-spline zonal representations of a wavefront generated by single actuator and experimentally measured is made for studying of zonal control possibilities and accuracy estimation.

For modal reconstruction basis a number of Zernike polynomials excluding piston term is taken, symmetrical representation is possible if taking all polynomials of a certain order, so for correct comparison we can use bases of first 5, 9, 14, 20, 27, 35, 44 etc. components.

For zonal fitting a product of 1-dimensional B-splines is used and basis functions are bell-shaped. Each basis function is centered in its control point, control points are positioned in a square array covering the complete pupil. Edge control points are chosen to be beyond the pupil area bounds. Number of B-spline basis functions is chosen to be congruous to Zernike mode number for a proper comparison of fitting quality. Position of control points for 21, 37, 45 and 76 B-spline basis functions is shown in Fig. 3.16



**Figure 3.16** Position of control points for 21, 37, 45 and 76 B-spline basis functions

Fitting quality is defined by RMS deviation of the reconstructed wavefront derivatives from fitted data against original values from wavefront sensor:

$$RMS = \frac{1}{N} \cdot \sqrt{\sum_{r=1}^N \left[ \left( \frac{\partial W_o}{\partial x} - \frac{\partial W_r}{\partial x} \right)^2 + \left( \frac{\partial W_o}{\partial y} - \frac{\partial W_r}{\partial y} \right)^2 \right]} \quad (26)$$

### 3.2.2. B-spline Reconstruction Accuracy Results

Results of wavefront reconstruction for experimentally generated wavefronts using 1, 2 and 3 actuators are shown in **Fig. 3.17**. Zernike decomposition is compared with cubic B-spline (4-th order polynomials) decomposition with close number of basis functions. Wavefronts without central symmetry and having local bumps are chosen for analysis.

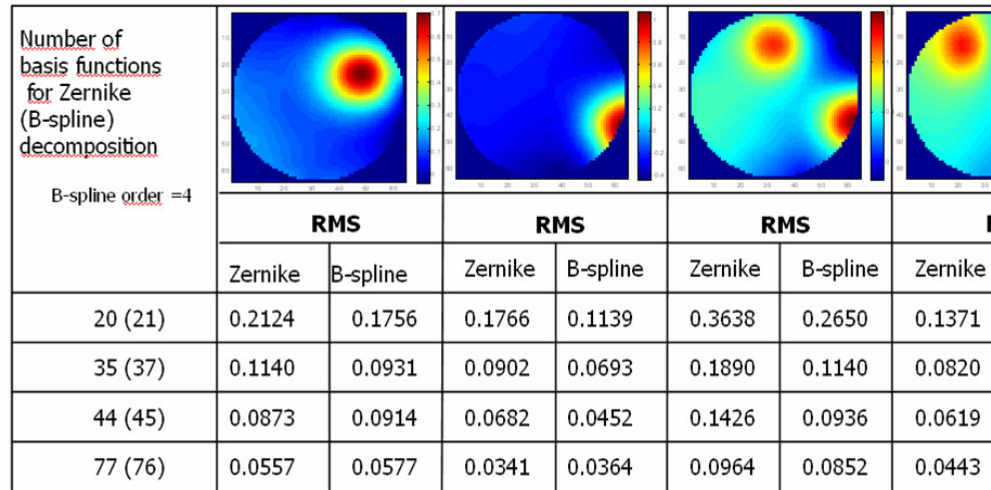


Figure 3.17

Reconstruction accuracy as a function of B-spline basis order was also studied and results for a complex wavefront can be seen in Fig.3.18

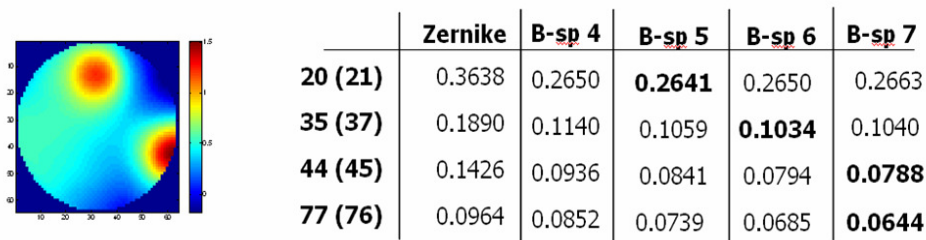


Figure 3.18

According to our results B-spline fitting has high accuracy for a wavefronts generated by PDM and in most situations provide better approximation than Zernike modal basis fitting. It is also a flexible method, open for parameters such as order and control points pattern optimization for a certain mirror or expected phasemap properties. It should also be mentioned that B-spline basis can be build for any shape of a pupil with equal accuracy and efficiency results.

### 3.2.3 Sparse MIF B-spline Representation

A set of actuator response functions forms so called matrix of influence functions (MIF). Initial MIF has a structure of a rectangular matrix with a number of columns equal to number of actuators and a number of rows double to sensor nodes number; measured MIF for our PDM matched with Shack-Hartmann sensor was shown in 3.2.1.

Influence functions of PDM were decomposed using B-spline basis, each of them is described with a set of 76 coefficients. Matrix of coefficients is presented in Fig.5.19a with

zero coefficients marked with blue color. Reordering of actuators makes it possible to concentrate zero coefficients in lower left and upper right corner (**Fig.5.19b**).

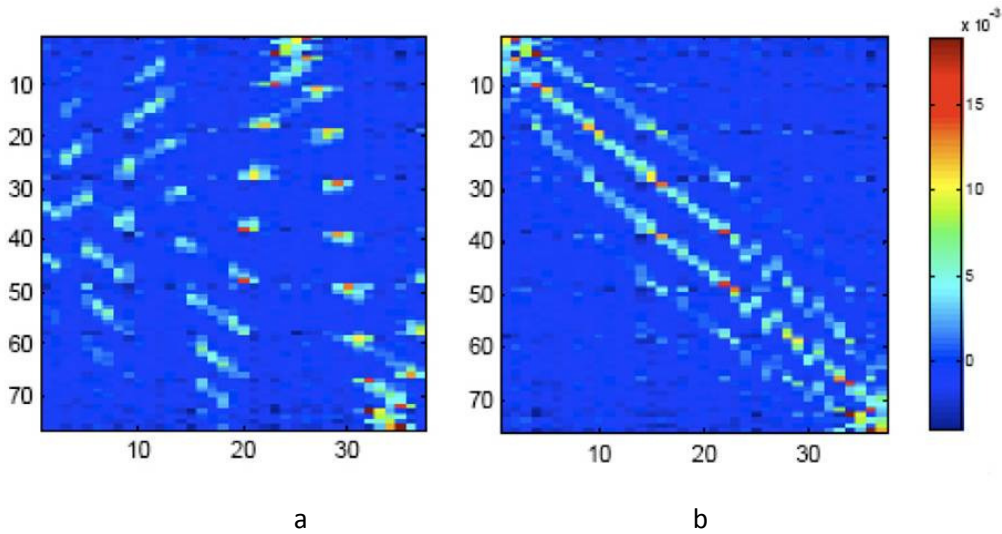


**Figure 3.19** MIF in B-spline basis before (a) and after (b) actuators reordering

Large number of matrix of influence function (MIF) coefficients with near-to-zero values allows to assume that it is possible to describe mirror response using only the most valuable basis functions with sufficient accuracy. Thus sparse matrix with significantly smaller number of non-zero coefficients can describe PDM response with accuracy comparable to fully populated matrix saving calculation time. Fully populated and sparse matrices are shown in **Fig. 3.20**.

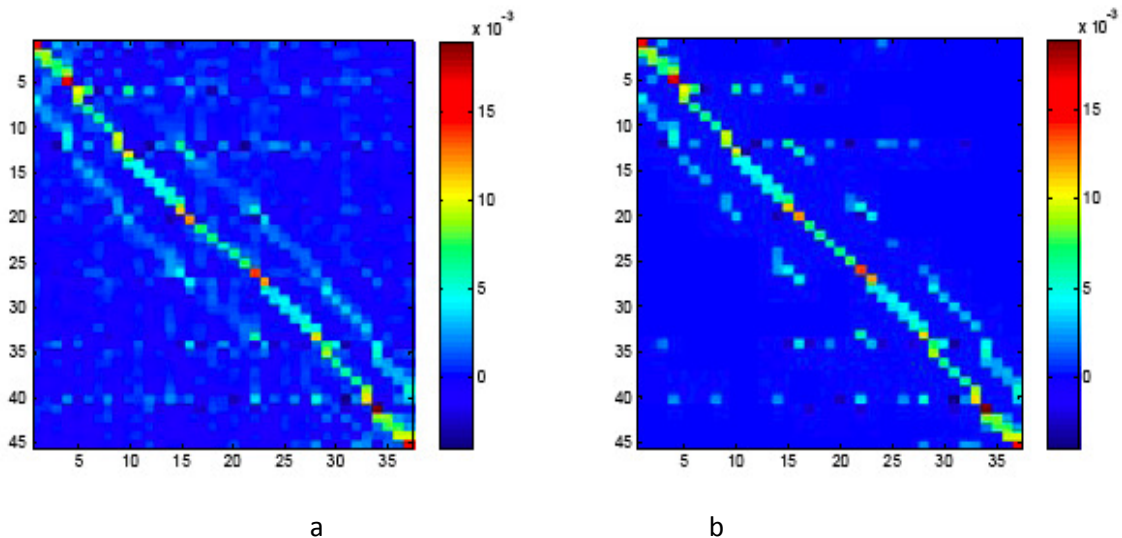


**Figure 3.20** MIF fully populated (a) and after sparsification (b)

Sparsification (setting non-valuable coefficients to zero) of MIF can be done in several different ways like setting a threshold or taking certain number of values. As far as reordered MIF has large zones of zero coefficients it can be useful to set zero values to whole zones within left lower and right upper zones of MIF (block method).

Response functions of central, zonal and edge actuators were measured and approximated by modal Zernike and zonal B-spline bases for 44-45 and 77-76 number of basis functions. Fully populated and sparse bases are used for B-spline decomposition. Three methods of sparsification were applied: 1) threshold 0.1: nulling of all coefficients smaller than 10% of maximum coefficient for a certain actuator, 2) representation with ten maximum coefficients for each actuator response and 3) block sparsification: based on coefficient position in reordered MIF, forming tridiagonal block matrix with all blocks out of tridiagonal set to zeroes; number of blocks is chosen to be 3x3 for 45 control points basis and 4x4 for 76 control points basis; automatic block partitioning depending on control points density and typical actuator effected zone is implemented in code. Number of non zero coefficients for different ways of sparsification can be seen in **Fig. 3.21**.

RMS fitting error is used as a measure of fitting accuracy.

	Actuator position				Response function				Control points
	RMS	non-zero components	RMS	non-zero components	RMS	non-zero components	RMS	non-zero components	
Zernike	0.138	44	0.106	44	0.0974	44	0.0503	44	
B-spline full	0.080	45	0.098	45	0.0693	45	0.0577	45	
B-spline sparse threshold 0.1	0.113	(45)	0.108	10(45)	0.0853	11(45)	0.1792	7(45)	
B-spline sparse 10 max.	0.115	10(45)	0.108	10(45)	0.0903	10(45)	0.1769	10(45)	
B-spline sparse blocks (Bn3)	0.080	45(45)	0.098	45(45)	0.0804	30(45)	0.0924	30(45)	
Zernike	0.0975	77	0.0682	77	0.0582	77	0.0263	77	
B-spline full	0.0809	76	0.0329	76	0.0277	76	0.0433	76	
B-spline sparse threshold 0.1	0.1345	15(76)	0.0931	14(76)	0.0996	12(76)	0.0799	11(76)	
B-spline sparse 10 max.	0.1784	10(76)	0.1278	10(76)	0.1258	10(76)	0.0981	10(76)	
B-spline sparse blocks (Bn4)	0.1044	57(76)	0.0423	57(76)	0.0477	38(76)	0.0543	38(76)	

**Figure 3.21**

**Accuracy of central, zonal and edge actuators response decomposition**

**using modal Zernike and zonal B-spline (full and sparse) bases.**

As can be seen even sparse B-spline fitting is able to provide more accurate representation compared do Zernike full matrix fitting.

### 3.3 PDM model

Simulation of a deformable piezoelectric mirror with a large number of actuators is required for testing the accuracy of the blok control method propose din this Thesis. The simulation of the behavior of a mirror with a large number of actuators will show the real capabilities of the technique. For numerical simulation of PDM behavior a thin plate bending model can be used. In this approximation deformation of the faceplate can be described by biharmonic equation

$$\Delta^2 \varphi(x, y) = p(x, y) / D \quad (18)$$

with  $D$  - cylindrical stiffness:

$$D = \frac{E}{12(1-\nu)} h^3. \quad (19)$$

For OKOTech PDM37:  $E = 7.2 \cdot 10^{10}$ ;  $h = 8 \cdot 10^{-4}$ ;  $\nu = 1.7 \cdot 10^{-1}$ .  $D = 3.70$

Force distribution  $p(x, y)$  has to satisfy static equilibrium conditions. This model assumes tip-tilt degrees of freedom in points of actuators attachment.

For a free edge plate solution of biharmonic equation can be found [Loktev 2006] in form:

$$S(z, \bar{z}) = \frac{1}{16\pi R} \sum_{i=1}^N P_i S(z, \bar{z}, \zeta_i, \bar{\zeta}_i) + S_0 + S_1 \operatorname{Re}(z) + S_2 \operatorname{Im}(z), \quad (26)$$

where

$$S(z, \bar{z}, \zeta, \bar{\zeta}) = (z - \zeta)(\bar{z} - \bar{\zeta}) \left\{ \ln(z - \zeta) + \ln(\bar{z} - \bar{\zeta}) + \frac{1-\mu}{3+\mu} [\ln(1 - z\bar{\zeta}) + \ln(1 - \bar{z}\zeta)] \right\} + \frac{(1-\mu)^2}{(1+\mu)(3+\mu)} z\bar{z}\zeta\bar{\zeta} + \frac{8(1+\mu)}{(1-\mu)(3+\mu)} [(1 - z\bar{\zeta}) \ln(1 - z\bar{\zeta}) + k(z\bar{\zeta}) + (1 - \bar{z}\zeta) \ln(1 - \bar{z}\zeta) + k(\bar{z}\zeta)], \quad (27)$$

with  $z$  and  $\zeta$  - coordinates in a complex valued form:

$$z = r \cos \varphi + ir \sin \varphi, \quad \zeta = \rho \cos \psi + i\rho \sin \psi$$

and  $k(x)$  - logarithmic integral

$$k(x) = \int_0^x \frac{\ln(1-\alpha)}{\alpha} d\alpha \quad (28)$$

For numerical calculations integral can be substituted with a sum:

$$\int_0^x \frac{\ln(1-\alpha)}{\alpha} d\alpha = -\sum_{k=1}^{\infty} \frac{x^k}{k^2} \approx -\sum_{k=1}^{100} \frac{x^k}{k^2}.$$

(29)

Forces  $P_i$  can be found from static equilibrium equations:

$$\begin{aligned}
 \sum P_i &= 0, \\
 \sum P_i x_i &= 0, \\
 \sum P_i y_i &= 0.
 \end{aligned}$$

(30)

and should be calculated due to voltages applied to actuators.

Described model was implemented in MatLab and shape of response functions for central and zonal actuators can be seen in **Fig. 3.22**.

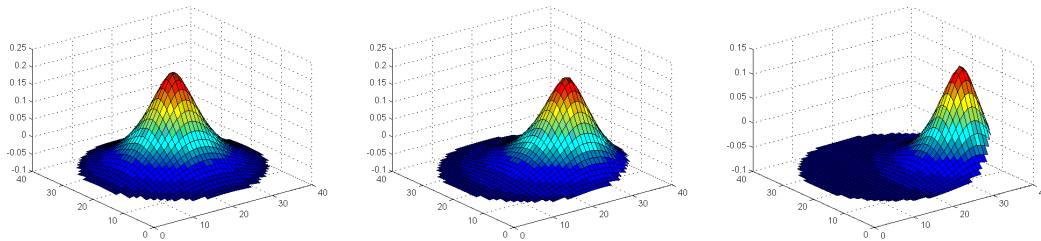


**Figure 3.22: Response functions in the PDM model**

Example of modeled surface with several commanded actuators can be seen in **Fig.3.23**.

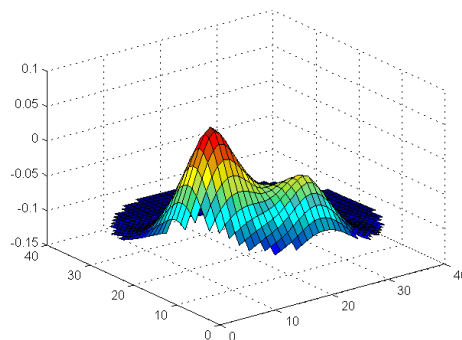


**Figure 3.23 Simulated PDM shape for voltages applied on 2 actuators**

Current PDM model has proved to be accurate enough for adaptive optics simulation, although point structure forces result in a more conical response functions than ones of real mirror. Extended zone of actuators contact with mirror can be simulated using finite element method for biharmonic equation solution, which is in process currently. Accurate numerical comparison of modeled and real response functions still to be done.

### 3.4 Construction of the turbulence generator

In our first approach, a liquid crystal programmable phase modulator (PPM) was intended to generate low-frequency turbulences by locally changing the induced phase maps in the liquid crystal, according to a Von-Karman turbulence profile. This required two main tasks: the implementation of a software enabling the generation of turbulence profiles according to Von Karman statistics, and the precise calibration and characterization of the PPM.

#### 3.4.1. Turbulence simulation.

The development of a software for the simulation of atmospheric turbulences on the PPM implied the calculation of Van Karman phase distributions varying with time. In addition, this enabled to set a full model of the experiment and to test offline the properties of the control techniques being implemented. With this purpose, a Matlab code for turbulence generation was implemented enabling the calculation of phase maps in a scale adequate for its future display on the PPM. Movies of phase distributions according to different turbulence levels ( $C_n$ ) were applied.

In order to simulate propagation through through turbulent media 2 independent phase screens using the Von Karman spectrum were used, to enable a realistic phase distribution calculation. An apodisation screen was placed in the middle of them at equidistant positions(fig.3.24), in order to mitigate the diffractive effects which appear due to the screen edges, which otherwise would induce artifacts in the exit pupil.

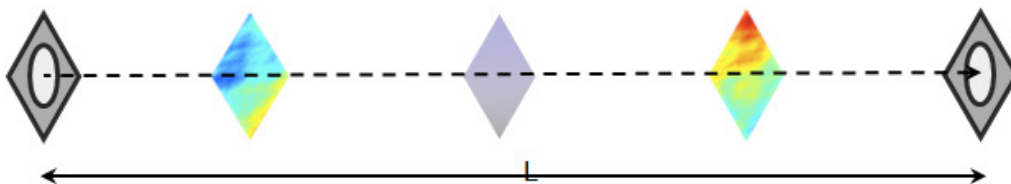
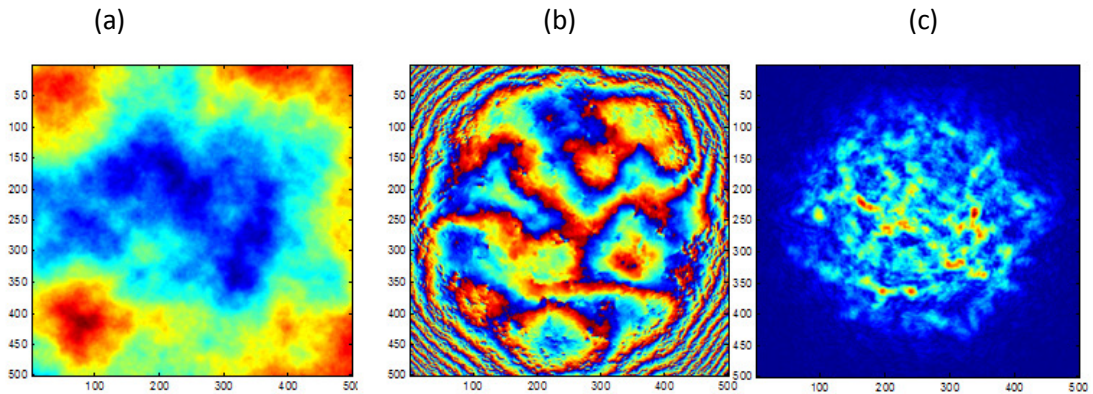


Figure 3.24 Configuration for turbulence simulation: double p

Thus, an arrangement with two phase screens with one apodisation screen in the middle was placed between an entrance and exit pupil of the turbulence pattern. Results for turbulence phase screens can be seen at fig.3.25. At the left a typical calculated Von Karman phase screen is shown. Next, the amplitude and phase distributions in a plane conjugate with the entrance pupil plane are presented showing the effects of turbulence.



**Figure 3.25 a) Von Karman single phase screen. (b) Amplitude and (c) phase at a pupil plane conjugate to entrance pupil**

Finally, and in order to validate the control algorithms in simulation conditions, the behavior of the complete optical setup including turbulence was implemented. With that purpose, the wavefront sensor pupil was conjugated with the apodization screen in order to simulate turbulence effects on the centroids of the sensor. This simulated spots have centroids which are obtained using the same algorithm used in the real experiment. A similar procedure was performed in order to show the effects of turbulence on the science camera. This enabled to simulate a complete feedback loop. Fig. 3.26 shows the images of the spots in the Shack-Hartmann plane, and at the science camera plane.

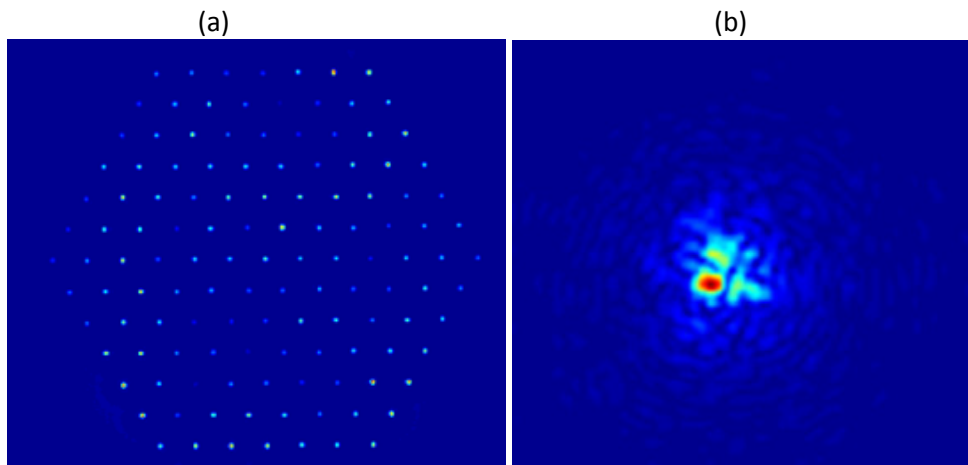


**Figure 3.26 Simulated turbulent image a) At the Shack-Hartmann sensor; b) At the science camera**

### 3.4.2 Active control of a liquid crystal programmable phase modulator (PPM)

The PPM was intended to be a key feature in the setup, as far as it enabled a large flexibility for the implementation of turbulent phase screens of different turbulence levels. In order to complete the test, an example of aberration generation for the null-testing of the aberrations induced in a progressive addition lens was implemented. This required a calibration stage, followed by the analysis of the aberration compensation capabilities of the unit.

### A. Phase modulation characteristics of the PPM

The PPM is an optically addressed phase modulator based on a parallel-aligned liquid crystal (PAL-LC), whose structure and operation has been described elsewhere [Li 1998]. In order to achieve a phase-only modulation, the incident wavefront needs to be linearly polarized in the direction of the parallel molecules of the liquid crystal when no electric field is applied. This is the normal working mode of the PPM, and the one used in the null test setup. However, to characterize the phase response of the PPM an amplitude modulation working mode is used (fig.3.27).

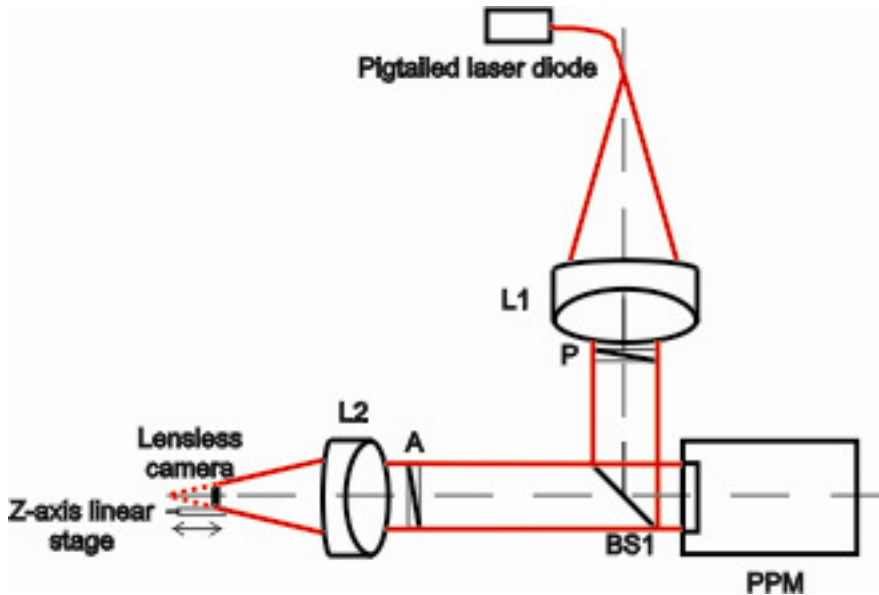


Figure 3.27 Setup for null test using a PPM, in the amplitude calibration mode.

The PPM is illuminated by a linearly polarized beam with axis oriented at 45 degrees from the axis of the molecules in the liquid crystal layer in unbiased state (meaning that polarizer P in Figure 1 is rotated 45 degrees), and a second polarizer A oriented orthogonally to polarizer P is inserted just after the PPM. In this configuration, changes in the light intensity transmitted by the second polarizer may be directly related to the cosine of the phase changes induced on the PPM. Induced phase changes are controlled by the grey level written onto the PPM, ranging from a full-screen null phase change when black (0), to a maximum phase change when white (255). Making the assumption of a linear relationship between the phase change  $\phi$  and the grey level G, the linear coefficient  $\alpha$  that relates the two parameters is evaluated by fitting a sinusoidal function to the transmitted intensity I for a series of uniform grayscale images displayed in the PPM, according to

$$I = \frac{I_{\max} + I_{\min}}{2} - \frac{I_{\max} - I_{\min}}{2} \cos(\alpha G + \alpha 2\phi_0) \quad (1)$$

where  $I_{\min}$  and  $I_{\max}$  are the minimum and maximum transmitted intensities, and  $\phi_0$  the phase of the PPM in the unbiased state. The intensity transmitted by the second linear polarizer is measured with a lensless CCD camera which images the PPM surface through doublet L2. With the aid of a Z-axis linear positioning stage, the CCD is accurately positioned close to the image focus of the doublet L2 in a position that fits the size of the CCD to the size of the light beam coming from the PPM. The PPM phase response is evaluated in the same conditions as it will perform the null correction in the experiment.

In order to characterize the phase modulation of the PPM, a set of 27 uniform grayscale maps ranging from 0 to 255 were written on it and the transmitted intensity was averaged

over the pixels of the lensless camera sensor. Consequently, potential nonuniformities in the diode laser beam, polarizers, doublets, camera sensor, and in the liquid crystal surface, were averaged and a global value for the coefficient that relates the phase change and the grey level is obtained, which is an usual procedure in this type of systems [Fernandez 2009][Gruneisen 2004]. Figure 3.28 shows the sinusoidal fit of the recorded intensity as a function of the graylevel displayed in the PPM. A linear coefficient  $\alpha = 0.0266 \pm 0.0003$  is obtained, allowing a phase modulation range of  $2.16\pi \pm 0.02\pi$  radians at  $\lambda = 635$  nm, equivalent to a path length variation of  $1.08 \pm 0.01$  wavelengths. The regression coefficient obtained (0.990) confirms the validity of the model in Equation 1.

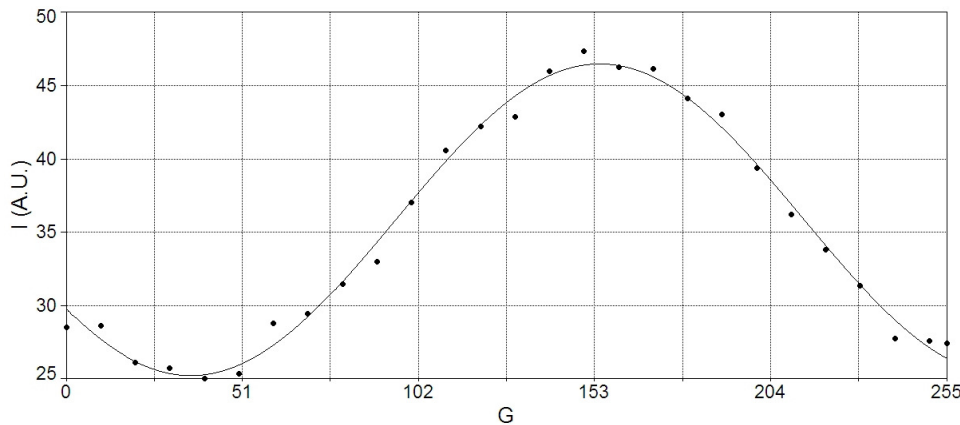


**Fig.3.28 . Sinusoidal fitting of the mean intensity (I) recorded by the camera sensor as a function of the uniform grey level maps (G) displayed in the PPM.**

#### B. PPM performance for aberration generation

Once the phase modulation response of the PPM has been calibrated, it is important to evaluate its capability for generating real aberrations within the active null test setup developed, when wrapped phase maps are used. With lens O removed from the active null test setup of Figure 1, ideal spherical phase maps of  $19.68\lambda$ ,  $39.36\lambda$  and  $78.72\lambda$  peak-to-valley height were displayed into the PPM and measured using a cylindrical Shack-Hartmann sensor (CSHWS), which extends the dynamic range of the aberrations measured [Ares 2007]. The quality of the aberrations generated by the PPM has been evaluated as the root mean squared (RMS) error between the ideal spherical phase map written in the PPM and the real spherical wavefront measured by the CSHWS. Results for ideal and real wavefronts are presented in Table 1. For the different amplitudes of defocus aberration analyzed, RMS errors stays below  $\lambda/18$ , showing the capability of the PPM for the generation of wavefronts in an open loop configuration, with no need of additional iterations.

Peak-to-valley amplitude (waves)	RMS error (waves)
19.68	0.024
39.36	0.029
78.72	0.054

In fact, results indicate the wavefront generation performance of the PPM within the null setup developed which includes the CSHWS, as far as the spherical wavefront is measured relative to a plane reference wavefront previously detected when a flat grayscale map is written in the PPM. Thus, potential deviations from flatness of the PPM surface might be practically cancelled in the Shack-Hartmann method, as far as these errors are present both in the aberrated and reference wavefronts [Neal 1997][Yoon 1996].

The ability of the PPM to reproduce the wavefront in a wrapped phase map representation allows the generation of large phase changes. However, in practice this becomes limited by the appearance of diffraction artifacts that become more significant as the amplitude of aberration to be generated increases. Reproducing steep phase changes with a small number of pixels considerably reduces the diffraction efficiency of the device, yielding light modulated by the PPM less intense than the unmodulated original wavefront. This creates a double image combining in different amounts the modulated (desired) and unmodulated (undesired) diffracted wavefronts. This behavior has been observed critical for spherical wavefronts with peak-to-valley heights from  $78.72\lambda$ , where the line patterns associated to the unmodulated original wavefront are significantly superimposed to those of the modulated spherical beam of interest and, as a consequence, the automatic line-tracking algorithm failed to process the image data. However, to overcome this problem which occurs when compensating large aberrations, a pinhole acting as a classical Fourier filter has been introduced in the null test setup, as it is described in the next Section.

### C. Null correction of a personalized progressive addition lens

To show the capabilities of the PPM as aberration generator it was tested as a null test system, in order to account for the total compensation of the wavefront transmitted by a commercial ophthalmic progressive addition lens (PAL), a real complex lens in the market. The PAL (Varilux Ipseo; Essilor International, France) with prescription RE + 0.00 Add + 2.00 had a design personalized for presbyopic wearers who mainly move their head and barely the eyes when performing a visual task. In order to evaluate the wavefront to be nulled, we firstly measured the wavefront transmitted by the PAL using the CSHWS and with the PPM acting as a mirror, and in a second step we made the null correction by displaying the corresponding conjugated phase map on the PPM. Due to the configuration of the system, the null test is accomplished for a central circular area of 20 mm of diameter of the lens, which contains the 16 mm length power progression corridor and part of the temporal and nasal sides. Figures 3.29a and b show the line patterns detected by the CSHWS and the reconstruction of the original wavefront transmitted by the PAL, respectively.

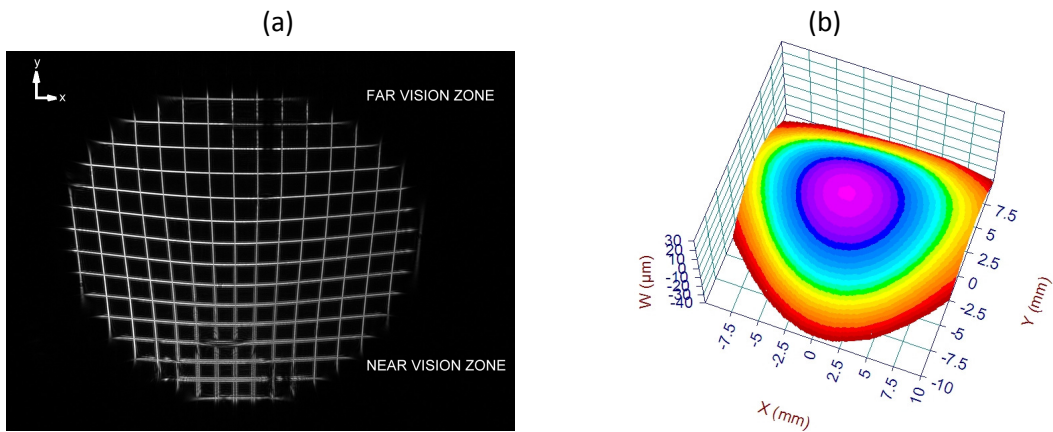


**Fig.3.29 . (a) CSHWFS pattern and (b) Reconstructed wavefront for a 0.0 Add 2.0 PAL lens.**

As expected, in the near vision region where the addition reaches + 2.00D, the width of the lines increases from the diffraction-limited size and are also considerably distorted. The wavefront shape for this lens has a total height change of over  $100\lambda$  peak-to-valley. Using the phase modulation constant obtained with the procedure described in the previous Section, the conjugated wavefront was calculated in a wrapped grayscale representation and displayed in the PPM in order to carry out the null correction. Due to the large aberrations involved, diffraction artifacts became noticeable so that the unmodulated original wavefront became superimposed to the desired plane wavefront obtained as a result of the null correction. Figure 3.30a shows the original complex line pattern image detected by the CSHWS. As it, the line processing algorithm is not able to properly identify the lines associated with the resulting plane wavefront. To solve this problem, a circular pinhole filter is introduced in the setup, centred with the optical axis of the PPM - CSHWS path and positioned in the image focal plane of the doublet L2 of the telescopic system. When the circular pinhole filter is introduced in the setup, the unmodulated wavefront becomes blocked and only the on-axis light corresponding to the resulting plane wavefront arrives at the CSHWS. Standard pinholes of diameters  $50\ \mu\text{m}$ ,  $100\ \mu\text{m}$ ,  $300\ \mu\text{m}$ ,  $500\ \mu\text{m}$  and  $1000\ \mu\text{m}$  have been experimentally tested, yielding the best performance the pinhole of  $300\ \mu\text{m}$ . The final reconstruction of the corresponding wavefront is depicted in Figure 3.30b. The RMS error from a perfect flat surface is of  $\lambda/12$ , which corresponds to a 0.08% of the peak-to-valley height of the original wavefront.

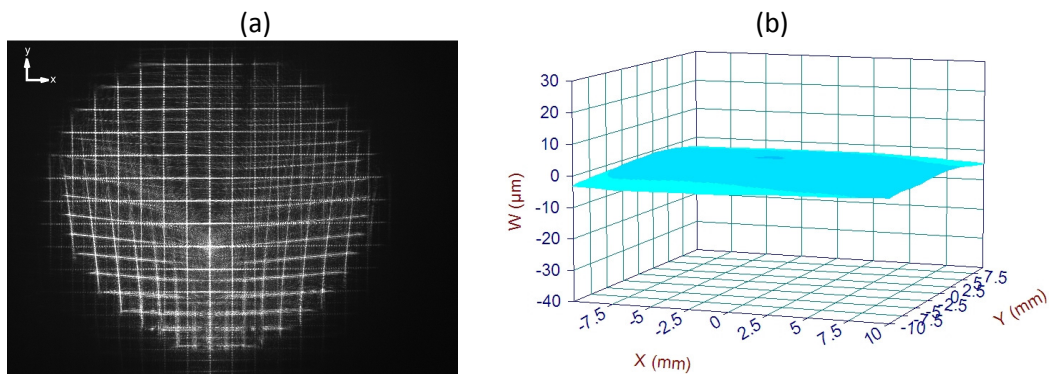


**Fig.3.29 . (a) CSHWFS pattern with PPM in aberration compensation and (b) Null test wavefront after PAL compensation and pinhole filtering for a 0.0 Add 2.0 PAL lens.**

### 3.5 Integration of the experimental setup

Once the simulation of the complete system was implemented, the control algorithms described in the Section 3.3 were validated in simulation. To have a complete simulation in experiment, a final experimental integration step was required. Figure 3.30 and 3.31 show two different views of the complete experimental setup. The different component may be appreciated in the system, including (in order) the light source, a water tank for real turbulence generation, the PPM, the deformable mirror, the SHWFS and the science camera. A number of different relay optics adapt the sizes of all components to yield a reliable system.

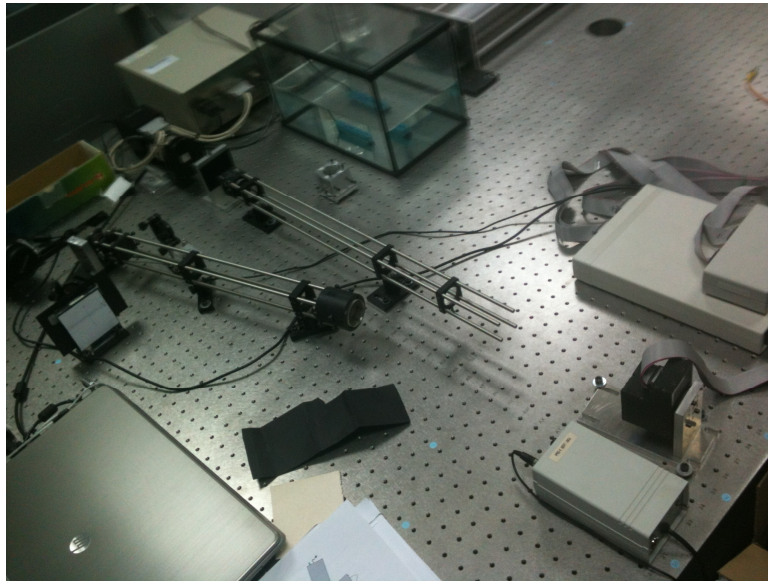


Fig.3.30 . Experimental setup. PPM is at the left, upper corner. Deformable mirror at the right, bottom



Fig.3.31 . Experimental setup. PPM at the left, lower corner. Science camera at the lower are, center. Deformable mirror at the right, upper area.

A water tank with a heater was added in order to test the effect of real natural turbulence in the system, over the simulated Von-Karman statistics which were used in the PPM experiment and the simulated control loop. Water instead of atmospheric turbulence was preferred due to the limited performance of the available computing system, while preserving the validation capabilities of the proposed control algorithm.

### 3.6 Block control algorithms

The main contribution of my PhD is the proposal of a block control algorithm approach which takes advantage of the sparsity of the control matrices used for adaptive optics. Control matrices are obtained as a compilation of the so-called influence functions of the actuators of a deformable mirror. That is, the effect of using a single actuator of the mirror and evaluating its effect in the shape of the surface of the mirror. Typically the surface changes are measured as direct slope information from the Shack-Hartmann sensor. This means the slopes in X and Y directions of each of the subapertures of the WFS are used to describe the surface changes. The list of all slope changes generates a vector in the matrix of influence functions, with length twice the number of lenslets in the Shack-Hartmann sensor (for slopes along X and Y).

By definition, most of the terms in this matrix of influence functions (MIF) are zero. That is, the matrix is intrinsically sparse, meaning that only a few terms have values different from zero. Figure 3.32 shows an image of a typical MIF, with blue being the value assigned to zero. Most terms are zero, and nonzero values are distributed more or less randomly across the matrix. The inversion of this matrix using singular value decomposition is a slow procedure, which becomes even slower when the number of actuators is very large. In this large actuator number case, matrices are even more sparse, as influence functions are more local and the number of lenslets larger to enable closing the loop.

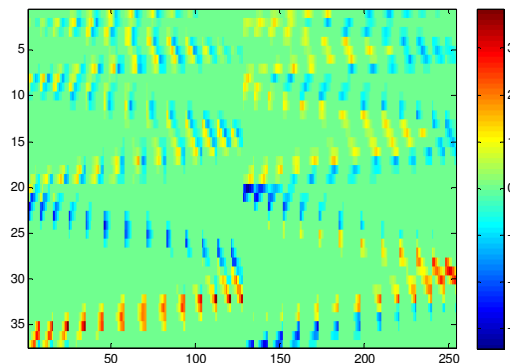


**Fig 3.32 MIF of a typical deformable mirror with 37 actuators. Most terms are zero.**

Due to this problem in size for the calculation of the pseudoinverse, several methods have been proposed, being specially successful the use of the iterative algorithms for solving the matrix. In iterative methods, normally,  $A$ , the MIF, is further sparsified for gaining speed and efficiency in real-time calculations (by using threshold when required), and no pseudoinverse is calculated. Instead, an equivalent function is set up which needs to be minimized. The solution in this case minimizes the function

$$f(a) = \frac{1}{2} a^T A^T A a + (A^T s)^T a + c$$

Where  $A$  is the MIF of the system, and the values of vector  $a$  which minimize the function become the solution for the MIF inversion. The classical algorithms for functions minimization, usual of optical design, for instance, may be used. The most extended one is gradient search/conjugated gradient, which normally is accompanied of some preconditioning to speed up convergence and taking advantage of the sparsified matrix, resulting in a nearly-diagonal  $A^T A$  matrix. A few iterations are usually enough to converge even for very large MIFs. This equation has the advantage of being iterative but also that the size depends on  $A^T A$ , which is a matrix with an almost diagonal shape than that of the original MIF.

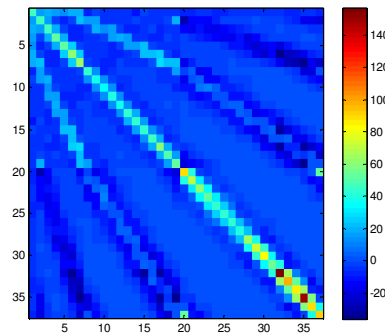


**Fig 3.33  $A^T A$  of a typical deformable mirror with 37 actuators. The matrix is almost diagonal.**

The proposal for block control is to apply a double preliminary step to speed the process even further. On one side, we propose to reorder  $A$ , the MIF of the system, so the reordering of the actuators gets most of the nonzero elements close to the diagonal. Once this is done, the matrix can be divided into tridiagonal blocks, which are very fast to invert due to their reduced and square sized. Fig.3.34 shows a tridiagonal matrix  $A$ . Inversion of tridiagonal blocks can be shown to be independent to other tridiagonal blocks, thus enabling parallelization of the calculation.

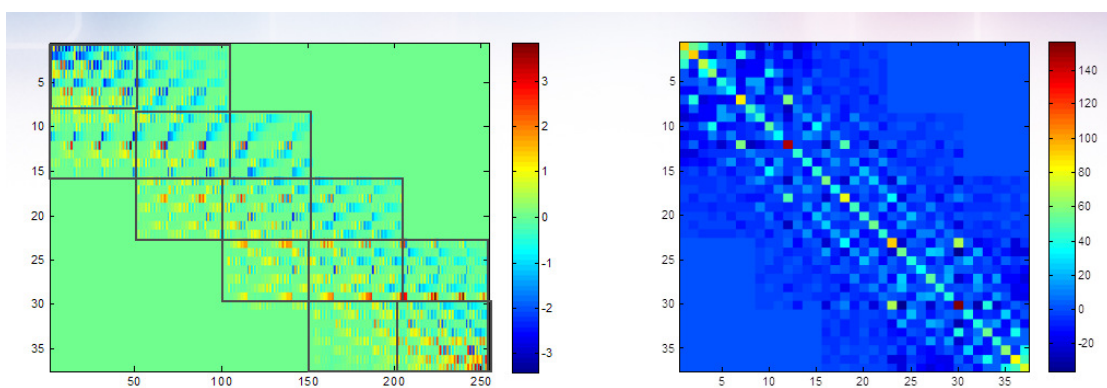


**Fig 3.34 Reordered matrix  $A$  divided into tridiagonal blocks, and corresponding  $A^T A$  for the 37 actuator case.**

The process speeds up the process as the zero terms are removed, and the matrix divided into a number of smallest tridiagonal matrices which may be computed in parallel. Figure 3.35 shows the comparison of the RMS value for the solutions obtained for compensation of wavefront aberrations, for two different levels of turbulence. It may be seen how the results obtained SVD (the classical, more accurate pseudoinverse method), conjugate gradient, and the proposed conjugate gradient blocks are comparable.

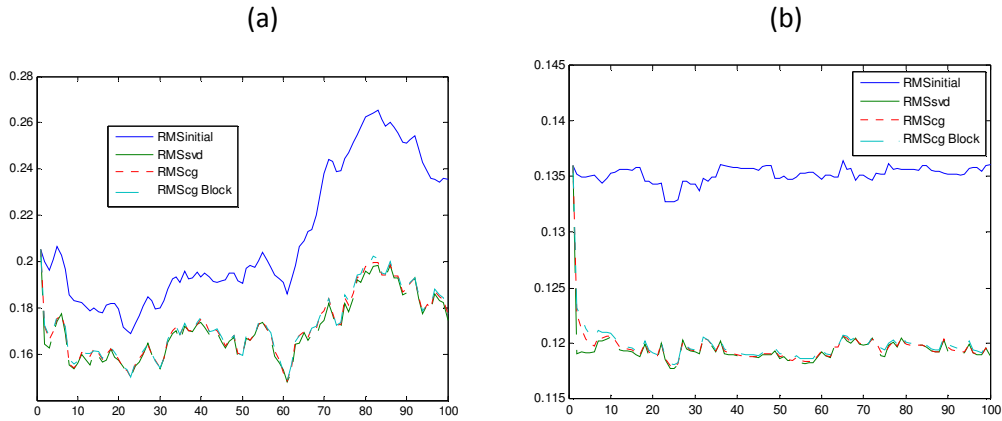


**Fig.3.35: Comparison of the rms values obtained using SVD, CG, and CG block for different simulated turbulence levels a)  $C_n^2=10^{-13}$ ; b)  $C_n^2=10^{-11}$**

Results may be seen to be comparable, while the CG gradient method was applied without iterations (direct solution) after a sparsification induced at 15% truncation. If the computational load of the matrix inversion using SVD is considered 100%, a conjugate gradient solution uses only 76% of the load and the block method we are proposing further reduces it to only 63%, without the use of any parallelization which would even further divide the used computational load.

Finally, the setup implemented in Fig 3.30 and 3.31 was used to further test the capabilities of the proposed control technique in different turbulence generation conditions. Results are compared for the different algorithms show equivalent performance, although the computational load of the block method we are proposing is the smallest of every one, and that is done before parallelization.

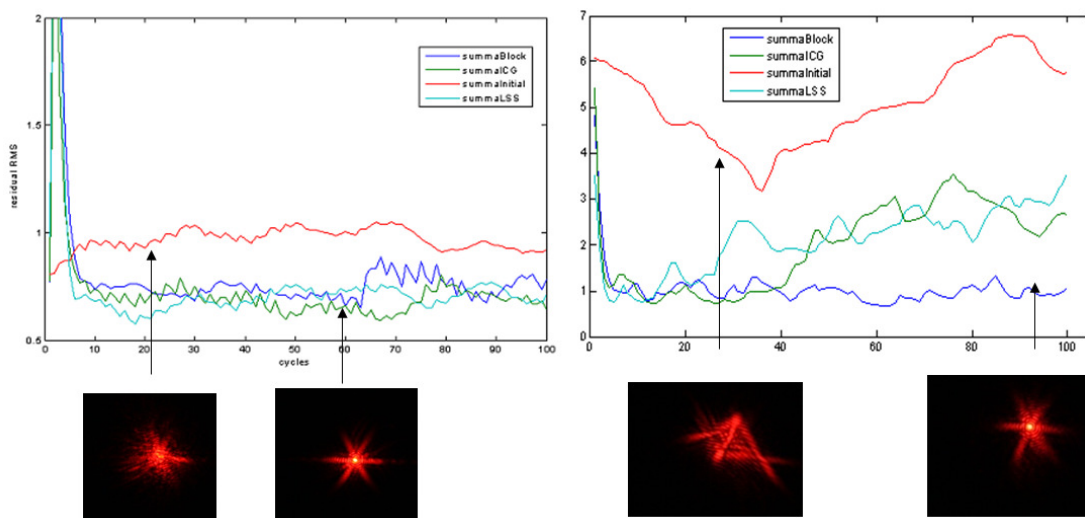


**Fig. 3.36: Experimental results**

In the first case, a Von Karmann statistics turbulence was graphed onto the PPM (as described in 3.4.1) and compensated actively using the system. The different algorithms were compared showing comparable performance. The second case is that of a moving plastic phase screen which induces larger aberrations. However, all cases are successfully managed by our proposed control algorithm, which delivers satisfactory performance with a much smaller computational load.

#### 4. Present situation

At present, the PhD Thesis is being prepared for its defence in Moscow, Russia, where the grantee has moved for personal reasons (maternity). The PhD lacks only the redaction of one publication with the description of the block control algorithm and its performance, which is currently under way, and the redaction of the memory, which, as may be seen in this memory, is quite structured and already complete, and just an issue of rephrasing and completing the different paragraphs. Defence of the PhD is expected along the summer of 2013, in Terrassa.

#### 5. Publications

M.Ares, S.Royo, I.Sergievskaya, J.Riu "Active optics null system based on a liquid crystal programmable spatial light modulator, Appl.Opt. 49 6201-6206 (2010)

I.Sergievskaya, S.Royo, M.Ares "B-Spline basis for adaptive piezoelectric mirror shape reconstruction" 7th International Workshop on Adaptive Optics for Industry and Medicine, Shatura (Russia), 8-11 Junio 2009. Comunicación Oral y publicación en actas del congreso.

M.Ares, S.Royo, I.Sergievskaya, "Active null test of personalized progressive addition lenses" 7th International Workshop on Adaptive Optics for Industry and Medicine, Shatura (Russia), 8-11 Junio 2009. Comunicación Oral y publicación en actas del congreso.

S.Royo, V.Suc, I.Sergievskaya, R.Atashkhouei, J.Segura, J.Galcerán, D.Panyella, J.Coll "Photogrammetric fringe projection for in-vivo skin topography measurements" 6ª Reunión Nacional de Optoelectrónica, Málaga, 15-17 Junio 2009. Poster y Actes del congrès (p 295-298)

I.Sergievskaya, S.Royo, M.Ares "B-Spline basis for adaptive piezoelectric mirror reconstruction" 9ª Reunión Nacional de Óptica, Ourense, 14-17 Setiembre 2009. Comunicación Oral y Actas del congreso (p.46)

M.Ares, S.Royo, I.Sergievskaya, R.Atashkhouei "Null test dinámico de lentes progresivas personalizadas basado en un modulador puro de fase de cristal líquido" 9ª Reunión Nacional de Óptica, Ourense, 14-17 Setiembre 2009. Comunicación Oral y Actas del congreso (p.65)

R.Atashkhouei, S.Royo, V.Suc, I.Sergievskaya, J.Segura, J.Galcerán, D.Panyella, J.Coll "Proyección de franjas fotogramétrica para la medida *in vivo* de topografías de piel humana. 9ª Reunión Nacional de Óptica, Ourense, 14-17 Setiembre 2009. Comunicación Oral y Actas del congreso (p.70)

Santiago Royo\*, Josep Arasa, Miguel Ares, Reza Atashkhouei, Francisco J.Azcona, Jesús Caum, Jordi Riu, Irina Sergievskaya, Vincent Suc "Nuevas líneas de trabajo en metrología óptica en el CD6 de la UPC". 10ª Reunión Nacional de Óptica, Zaragoza, 4-7 Setiembre 2012. Póster y Actas del congreso

## 6. Bibliography

- [Ares 2006] M.Ares, S.Royo, "Comparison of cubic B-spline and Zernike-fitting techniques in complex wavefront reconstruction" *Appl.Opt.*, v.45(27), 6954-6964 (2006).
- [Ares 2007] M. Ares, S. Royo, and J. Caum, "Shack-Hartmann sensor based on a cylindrical microlens array", *Opt. Lett.* **32(7)**, 769-771 (2007).
- [Axelsson 1977] O.Axelsson, *Solution of linear systems of equations: iterative methods*. Springer Berlin / Heidelberg, 1977.
- [Bardsley 2008] J.M.Bardsley. *Wavefront reconstruction methods for adaptive optics systems on ground-based telescopes*. *SIAM Journal on Matrix Analysis and Applications*, v.30 (1), 67-83, 2008.
- [Basden 2007] A.Basden, R.Myers, R.Wilson, T.Butterley, M.Harrison. *Adaptive optics simulations for extremely large telescopes*. Adaptive Optics: Analysis and Methods (AO), Vancouver, Canada, 2007.
- [Bechhoefer 2005] J.Bechhoefer. *Feedback for physicists: A tutorial essay on control*. *Reviews of modern physics*, v.77, 783-836, 2005
- [Bücker 2002] H.M. Bücker. *Iteratively solving large sparse linear systems on parallel computers "Quantum Simulations of Complex Many-Body Systems: From Theory to Algorithms, Lecture Notes, NIC Series, Vol. 10, pp. 521-548, 2002."*
- [Chanan 2004] G.Chanan, D.MacMartin, J.Nelson, T.Mast. *Control and alignment of segmented-mirror telescopes: matrices, modes, and error propagation*. *Appl.Opt.*, v.43(6), 1223-1232, 2004.
- [Cuthill 1969] E.Cuthill, J.McKee. *Reducing the bandwidth of sparse symmetric matrices* "in 'Proc. of the 24th National Conference of the ACM'. Brandon Systems Press, 1969."
- [Dessenne 1998] C.Dessenne, P.-Y. Madec, G.Rousset. *Optimization of a predictive controller for closed loop adaptive optics*. *Appl.Opt.*, v.37(21), 4623-4633, 1998.
- [Dubra 2007] A.Dubra. *Wavefront sensor and wavefront corrector matching in adaptive optics*. *Optics Express*, v.15(6) 2762-2769, 2007.
- [Ellerbroek 1986] B.L.Ellerbroek. *Comparison of least squares and minimal variance wavefront reconstruction for turbulence compensation in the presence of noise*. Rep.TR721R (Calif. 1986).
- [Ellerbroek 1994] B.L.Ellerbroek, C.V.Loan, N.P.Pitsianis, R.J.Plemmons. *Optimizing closed-loop adaptive optics performance with use of multiple control bandwidths*. *J.Opt.Soc.Am.A*, v.11(11),2871-2886, 1994.
- [Ellerbroek 2002] B.L.Ellerbroek, *Efficient computation of minimum-variance wave-front reconstructors with sparse matrix techniques*. *J.Opt.Soc.Am.A*, v.19(9), 1803-1816, 2002.
- [Ellerbroek 2003] B.L.Ellerbroek, C.R.Vogel. *Simulations of closed-loop wavefront reconstruction for multi-conjugate adaptive optics on giant telescopes*. *Proc.SPIE 5169-23*, (2003), 206-217.
- [Ellerbroek 2009] B.L. Ellerbroek, C.R. Vogel. "Inverse Problems in Astronomical Adaptive Optics" *Inverse Problems*, v. 25(6),2009.
- [Fernandez 2009] E. J. Fernández, P. M. Prieto, and P. Artal, "Wave-aberration control with a liquid crystal on silicon (LCOS) spatial phase modulator", *Opt. Express* 17(13), 11013-11025 (2009).
- [Fraanje 2009] N. Doelman, R. Fraanje, P. Massioni, M. Verhaegen. *Computationally Efficient Control Strategy for Large Adaptive Optics Systems*. Presented on AO4ELT, Paris, June 2009.  
[http://ao4elt.lesia.obspm.fr/abstract\\_162.html](http://ao4elt.lesia.obspm.fr/abstract_162.html)
- [Fried 1977] D.L.Fried. *Least-square fitting of a wave-front distortion estimate to an array of phase-difference measurements*. *J.Opt.Soc.Am.*, v.67, 370-375, 1977.
- [Gendron 1994] E.Gendron, P.Lena. *Astronomical adaptive optics. I. Modal control optimization*. *Astron.Astrophys.* 291 337-347, 1994.
- [Gilles 2001] L.Gilles, C.R.Vogel, B.L.Ellerbroek. *Iterative algorithms for large scale wave front reconstruction in Signal Recovery and Synthesis*, 2001 OSA Technical Digest Series, SWA3.
- [Gilles 2003] L.Gilles. *Order-N sparse minimum-variance open-loop reconstructor for extreme adaptive optics*. *Optics Letters*, v.28 (20) 1927-1929, 2003.
- [Glindemann 1993] A.Glindemann, R.G.Lane, J.C.Dainty, *Simulation of time-evolving speckle patterns using Kolmogorov statistics*. *J. of Modern Optics*, v.40(12) 2381-2388, 1993.
- [Goodman 1985]J.W.Goodman, *Statistical optics* John Wiley, New York, 1985.

- [Gruneisen 2004] M. T. Gruneisen, L. F. DeSandre, J. R. Rotge, R. C. Dymale, and D. L. Lubin, "Programmable diffractive optics for wide-dynamic-range wavefront control using liquid-crystal spatial light modulators", *Opt. Eng.* **43** (6), 1387-1393 (2004).
- [Hardy 1977] J.W.Hardy, J.E.Lefebvre, C.L.Koliopoulos. Real time atmospheric compensation. *J.Opt.Soc.Am.*, v.67(3), 360-369, 1977.
- [Hardy 1998] J.W.Hardy . Adaptive optics for astronomical telescopes. New York: Oxford, 1998
- [Hinnen 2007] K.Hinnen, M.Verhaegen, N.Doelman. Exploiting the spatiotemporal correlation in adaptive optics using data-driven H2-optimal control. *J.Opt.Soc.Am.A*, v.24(6), 1714-1724, 2007.
- [Hu 2009] L.Hu, L.Xuan, D.Li, Zh.Cao, Q.Mu, Y.Liu, Z.Peng, X.Lu. Real-time liquid-crystal atmosphere turbulence simulator with graphic processing unit. *Optics Express*, v.17 (9) 7259-7268, 2009.
- [Ishimaru 1978] A.Ishimaru. Wave propagation and scattering in random media. New York: Academic, 1978.
- [Lee 2006] L.H.Lee. Loopshaped wavefront control using open-loop reconstructors. *Optics Express*, v.14(17) 7477-7486, 2006.
- [Li 1998] H. Li, N. Mukohzaka, N. Yoshida, Y. Igasaki, H. Toyoda, T. Inoue, Y. Kobayashi, and T. Hara, "Phase modulation characteristics analysis of optically-addressed parallel-aligned nematic liquid crystal phase-only spatial light modulator combined with a liquid crystal display", *Opt. Rev.* **5**(3), 174-178 (1998).
- [Loktev 2006] M.Loktev, O.Soloviev, G.Vdovin, Adaptive Optics Product Guide, Flexible Optical BV (OKO Technologies), 2006.
- [Lurie 2000] B.J.Lurie, P.J.Enright. Classical feedback control with MatLab. Marcel. Dekker, Inc., New York, NY 2000.
- [MacMartin 2003] D.G.MacMartin, Local, hierarchic, and iterative reconstructors for adaptive optics. *J.Opt.Soc.Am.A*, v.20(6), 1084-1093, 2003.
- [Miller 1999] D.W.Miller, S.C.O.Grocott. Robust control of the Multiple Mirror Telescope adaptive secondary mirror. *Opt.Eng.* 38(8) 1276-1287, 1999.
- [Montilla 2009] I.Montilla, C.Bechet, M.LeLouran, C.Correia, M.Tallon, M.Reyes, E.Thiebaut. Comparison of Reconstruction and Control algorithms on ESO end-to-end simulator OCTOPUS. Presented on AO4ELT, Paris, June 2009.  
[http://ao4elt.lesia.obspm.fr/abstract\\_186.html](http://ao4elt.lesia.obspm.fr/abstract_186.html)
- [Murphy 2001] T.P.Murphy, R.G.Lyon, J.E.Dorband, J.M.Hollis. Sparse matrix approximation method for an active optical control system. *Appl.Opt.*, v.40(35), 6505-6514, 2001.
- [Neal 1997] D. R. Neal, D. J. Armstrong, and W. T. Turner, "Wavefront sensors for control and process monitoring in optics manufacture", in *Lasers as Tools for Manufacturing II*, Proc. SPIE, **2993**, 211-220 (1997).
- [Neal 2002] D.R.Neal, J.Copland, D.Neal. Shack-Hartmann wavefront sensor precision and accuracy. *Proc.SPIE* 4779, 148-160, 2002.
- [Nicolle 2004] M.Nicolle, T.Fusco, G.Rousset, V.Michau. Improvement of Shack-Hartmann wave-front sensor measurement for extreme adaptive optics. *Optics Letters*, v.29(23), 2743-2745, 2004.
- [Panagopoulou] S.I.Panagopoulou, D.R.Neal. Zernike vs. zonal matrix iterative wavefront reconstructor.
- [Perez 2004] D.G.Perez, L.Zunino, M.Garavaglia. Modeling turbulent wave-front phase as a fractional Brownian motion: a new approach. *J.Opt.Soc.Am.A*, v.21(10), 1962-1969, 2004.
- [Poyneer 2002] L.A.Poyneer, D.T.Gavel, J.M.Brasc. Fast wave-front reconstruction in large adaptive optics systems with use of Fourier transform. *J.Opt.Soc.Am.A*, v.19(10), 2100-2111, 2002.
- [Raymond 2008] T.D.Raymond, D.R.Neal, A.Whitehead, G.Wirth. High speed smart CMOS sensor for adaptive optics. Adaptive Optics for industry and medicine proc., 2008.
- [Reid 2005] J.K.Reid, J.A.Scott. Reducing the total bandwidth of a sparse unsymmetric matrix SIAM J. Matrix Anal. Appl. 28, 805-821 (2005).
- [Reif 1998] J.H.Reif. Efficient approximate solution of sparse linear systems. *Computers Math. Applic.* v.36(9), 1998, 37-58.
- [Roggemann 1996] M.C.Roggemann, B.M.Welsh. Imaging through turbulence. CRC Press, Boca Raton, FL, 1996.
- [Roggemann 1997] M.C.Roggemann, B.M.Welsh, R.Q.Fugate Improving the resolution of ground-based telescopes *Reviews of modern physics*, v.69(2), 437-505, 1997



- [Saad 2000] Y.Saad, H.A.van der Vorst. Iterative solution of linear systems in the 20th century. *J. of Computational and Applied Mathematics* 123 (2000) 1-33.
- [Shi 2002] F.Shi, D.MacMartin, M.Troy, G.L.Brack, R.S.Burruss, T.Truong, R.Decany. Local wavefront reconstruction: simulation, experiments and predictions.
- [Shi 2003] F.Shi, D.MacMartin, M.Troy, G.L.Brack, R.S.Burruss, R.Decany. Sparse matrix wavefront reconstruction: simulations and experiments. *Proc.SPIE v.4839*, (2003), 1035-1044.
- [Song 2009] H.Song, G.Vdovin, R.Fraanje, G.Schitter, M.Verhaegen. Extracting hysteresis from nonlinear measurement of wavefront-sensorless adaptive optics system. *Optics Letters*, v.34(1) 61-63, 2009.
- [Southwell 1980] W.H.Southwell. Wave-front estimation from wave-front slope measurements. *J.Opt.Soc.Am.*, v.70(8), 998-1006, 1980.
- [Sriram 2007] V.Sriram, D.Kearney, An ultra fast Kolmogorov phase screen generator suitable for parallel implementation. *Optics Express*, v.15(21) 13709-13714, 2007.
- [Timoshenko 1959] S.P.Timoshenko, S.Woinowsky-Krieger, *Theory of Plates and Shells*, McGraw-Hill, 1959.
- [Truong 2002] T.Truong, M.Troy, G.Brack, T.Trinh, F.Shi, R.Decany. Real time wavefront processors for the next generation of adaptive optics systems: a design and analysis. in *Adaptive Optical System Technologies II*, P. L. Wizinowich and D. Bonaccini, eds., *Proc. SPIE 4839*, 911-922 (2002).
- [Tyson 2000] R.K.Tyson, *Introduction to Adaptive Optics*, SPIE Press, 2000.
- [Vogel 2004] C.R.Vogel. Sparse Matrix Methods for Wavefront Reconstruction Revisited "SPIE 5490-60, *Advancements in Adaptive Optics* (2004), pp. 1327-1335."
- [Vuik 2008] C.Vuik. Iterative solution methods
- [Wallner 1983] E.P.Wallner. Optimal wave-front correction using slope measurements. *J.Opt.Soc.Am.*, v.73(12), 1771-1776, 1983.
- [Welsh 1997] B.M.Welsh. A Fourier series based atmospheric phase screen generator for simulating nonisoplanatic geometries and temporal evolution. *Proc.SPIE3125*, (1997), 327-338.
- [Wild 1995] W.J.Wild, E.J.Kibblewhite, R.Vuilleumier. Sparse matrix wave-front estimators for adaptive-optics systems for large ground-based telescopes. *Optics Letters*, v.20 (9) 955-957, 1995.
- [Yoon 1996] G.Y. Yoon, T. Jitsuno, M. Nakatsuka, and S. Nakai, "Shack-Hartmann wave-front measurement with a large F-number plastic microlens array", *Appl. Opt.* **35 (1)**, 188-192 (1996).